

Case Report

Non-local piezoelectricity to incorporate the influence of small-scale factors on the resonance behavior of the Mindlin piezoelectric polymeric nanoplates

Narinderjit Singh Sawaran Singh^a, Waqed H. Hassan^{b,c}, Zainab Mohammed Ameen Ahmed^d, Younis Mohamed Atiah Al-zahy^e, Soheil Salahshour^{f,g,h}, Mostafa Pirmoradian^{i,*}

^a Faculty of Data Science and Information Technology, INTI International University, Persiaran Perdana BBN, Putra Nilai, Nilai, 71800, Malaysia

^b University of Warith Al-Anbiyaa, Kerbala, 56001, Iraq

^c Department of Civil Engineering, College of Engineering, University of Kerbala, Kerbala, 56001, Iraq

^d Department of basic sciences, College of Nursing, university of kirkuk, Iraq

^e Department of Physics, College of Education, Misan University, Maysan, Iraq

^f Faculty of Engineering and Natural Sciences, Istanbul Okan University, Istanbul, Turkey

^g Faculty of Engineering and Natural Sciences, Bahcesehir University, Istanbul, Turkey

^h Faculty of Science and Letters, Piri Reis University, Tuzla, Istanbul, Turkey

ⁱ Department of Mechanical Engineering, Khomeinishahr branch, Islamic Azad University, Khomeinishahr, Iran



ARTICLE INFO

Keywords:

Vibration resonance
Piezoelectric polymeric material
Elastic nanoplate
Moving nanoparticle
Incremental harmonic balance method

ABSTRACT

This study presents an investigation into the vibration resonance of Mindlin piezoelectric polymeric nanoplates under electromechanical loading, particularly in the presence of a rotating nanoparticle. The novelty of this research lies in the application of non-local piezoelectricity, which effectively incorporates the influence of small-scale factors on the resonance behavior of the nanoplate. By employing a variational approach to derive the governing equations, this work advances the understanding of how various parameters such as the non-local parameter, dimensions of the nanoplate, excitation voltage, and mass of the nanoparticle affect resonance frequencies. The Galerkin method is utilized to solve the partial differential equations governing the dynamics of the piezoelectric polymeric nanoplate, marking a significant methodological contribution to the field. The incremental harmonic balance approach is then applied to estimate the system's resonance frequencies, with numerical simulations confirming their existence. This research not only elucidates the complex interactions affecting resonance behavior but also highlights the potential for optimizing the design of nanostructures in various applications, including sensors and energy-harvesting devices. The findings suggest that increasing the non-local parameter softens the nanoplate's rigidity, leading to decreased resonance frequencies, while modifications in dimensions and applied voltages can enhance these frequencies. Overall, this study lays the groundwork for future explorations into the dynamic behavior of piezoelectric materials, emphasizing the importance of small-scale effects in nanotechnology applications.

1. Introduction

Due to their distinctive property of converting mechanical and electrical energy, piezoelectric materials find extensive application in actuators and sensors that regulate a variety of engineering systems. Consequently, contemporary research is extremely interested in the investigation of the behavior of these materials. In recent years, there has been significant interest in the utilization of piezoelectric materials

within nanostructures, including nanoplates, nanowires, and nanotubes, due to the widespread trend toward compact devices across industries. Among these nanostructures, nanoplates are utilized extensively in numerous fields of mechanical engineering [1,2]. Capacitors, power relays, thin films, molecular sensors, and nano- and micro-electromechanical systems all make use of nanoplates [3]. When dynamic loads are applied to nanoplates, resonance may occur, leading to their eventual failure. Consequently, the determination of the factors

* Corresponding author.

E-mail address: m.pirmoradian@iaukhsh.ac.ir (M. Pirmoradian).

<https://doi.org/10.1016/j.cscee.2025.101125>

Received 3 January 2025; Received in revised form 28 January 2025; Accepted 29 January 2025

Available online 30 January 2025

2666-0164/© 2025 The Authors. Published by Elsevier Ltd. This is an open access article under the CC BY license (<http://creativecommons.org/licenses/by/4.0/>).

that influence the resonance frequencies of nanoplates, in addition to their calculation and evaluation, are important topics in the scientific literature. In the investigation of elastic nanoplates, numerous hypotheses have been proposed thus far. In general, investigations are carried out utilizing two-dimensional elasticity theories or alternative three-dimensional elasticity theories. Although investigations conducted utilizing the theory of three-dimensional elasticity are fundamental and accurate, the application of this approach presents several complexities and obstacles. To address these difficulties, a multitude of theories have been proposed; nevertheless, the precision of these theories is contingent upon the number of terms integrated into the displacement field expansion [4]. Kirchhoff's plate theory fails to account for the influence of shear strains, rendering it insufficiently precise when applied to thick nanoplates [5,6]. The purpose of developing Mindlin's plate theory was to rectify this inadequacy and enhance precision [7,8]. A theory that incorporates the consequences of shear deformation serves as a supplementary framework to Kirchhoff's theory. Researchers frequently employ experiments and molecular dynamics (MD) simulations to analyze the behavior of nanostructures. The exorbitant computational expense and intricacy of MD simulations limit their application to systems comprising a scarce number of atoms and molecules. Furthermore, nanoscale investigations are challenging and expensive. As a result, theoretical frameworks are commonly utilized to achieve this objective. Efficient methods for examining the mechanical behavior of nanostructures, such as bending, buckling, and free and forced vibrations, are proposed by the theory of continuum mechanics. The ability of classical continuum mechanics to forecast mechanical behavior that is dependent on scale is limited. As a consequence of this constraint, scholars have put forth revised frameworks, including the modified couple stress theory [9,10], the non-local elasticity theory [11], and the non-local strain gradient theory [12]. These revised theories account for size-dependent effects. The conventional theory of continuum elasticity posits that tension and strain at every point are directly proportional. Researchers have conducted considerable research and investigations on nanoplates, nanoshells, nanorods, and nanobeams based on this foundation. The investigation of the thermo-mechanical deformation of nanoplates in hygro-thermal environments was conducted by Alzahrani et al. [13]. Simsek and Yurtcu [14] resolved the issue of buckling and bending behavior in functionally graded Timoshenko nanobeams. Hosseini-Hashemi et al. [15] examined the spontaneous vibration of rectangular nanoplates in a separate investigation. Sobhy [16] utilized the two-variable plate theory to analyze multilayer graphene sheets. Chen et al. [17] investigated wave propagation in periodic layered nanostructures. Liu et al. [18] examined the post-buckling and nonlinear vibration of piezoelectric nanobeams subjected to thermo-electro-mechanical loading by employing the non-local theory. Sayyad and Ghugal [19] investigated the free vibrations and bidirectional deformation of thick plates. In their study of the vibration and flexural deformation of non-local piezoelectric nanobeams, Eltaher et al. [20] looked into surface effects. Zarepour et al. [21] investigated nanobeam post-buckling and nonlinear vibration. Liu et al. [22] utilized the non-local Mindlin plate theory to examine the nonlinear vibrations of piezoelectric nanoplates subjected to thermo-electric loading. A new study by Ebrahimi et al. [23] used the non-local theory to look into how magneto-electro-piezo nanobeams on the Winkler-Pasternak foundation bend when they are put under hygro-thermal loads. Using non-local theory, Mazur and Awrejcewicz [24] looked into how orthotropic nanoplates move when they are hit by an in-plane magnetic field. Pirmoradian et al. [25,26] investigated the non-local parametric resonance of carbon nanotubes and graphene sheets that were excited by moving nanoparticles. Smart polymeric materials consisting of polyvinylidene fluorides (PVDF) also exhibit ferroelectric, piezoelectric, and pyroelectric characteristics. Furthermore, this semi-crystalline polymer possesses numerous advantageous qualities, such as exceptional flexibility, minimal weight, thermal stability, resistance to chemicals, and the capability to be produced in

significant volumes. As a result, they are highly compatible with sensors spanning a range of scales. To ascertain the integrity of PVDF nanoplate-based nanoelectromechanical sensors, an analysis of the nanoplates' vibration in response to various excitations, including nanoparticles and external mechanical stresses, is imperative. Investigating the dynamic characteristics of these materials at the nanoscale has emerged as a highly captivating field of study among scholars in recent times. The study conducted by Arani Ghorbanpour et al. [27] examined the dynamic behavior of PVDF nanoplates that were excited by a nanoparticle in motion on a Pasternak substrate. Haghshenas and Ghorbanpour Arani [28] investigated the effect of stationary nanoparticles on the non-local vibration of PVDF nanoplates. Ebrahimi and Barati [29] also looked into how smart piezoelectric polymeric nanoplates that are supported only on a viscoelastic substrate can dampen oscillations. They analyzed the effects of applied voltage, foundation viscoelasticity, length scale, nonlocal parameters, and Winkler-Pasternak parameters. Despite the existence of several investigations about the estimation of the natural frequencies of PVDF nanoplates [29] and their dynamic response to nanoparticles [27,28], the aforementioned studies remain insufficient. Thus, it is necessary to conduct an inquiry into the resonance states exhibited by PVDF nanoplates and devise methods to control their undesired vibrations. This study presents the initial investigation of the resonance frequencies exhibited by a piezoelectric polymeric nanoplate made of PVDF material situated on an elastic medium. The nanoplate is subjected to biaxial stress, electrical voltage, and the motion of nanoparticles. In the model presented in this study, a biomolecule, buckyball, or virus traverses a piezoelectric nanoplate, serving as an illustration of a mass sensor. The nanoplate is represented through the integration of Eringen's non-local elasticity theory and Mindlin plate theory. Following the construction of the motion equations using Hamilton's principle, the time-varying matrices of mass, stiffness, and damping are acquired. By employing the incremental harmonic balance (IHB) method, the resonance frequencies are computed. An exhaustive investigation is conducted into the effects of numerous variables on resonance frequencies, such as nanoplate size, non-local parameters, external voltage, nanoparticle mass, biaxial stress, vibrational mode number, and foundation rigidity. In addition, numerical simulations validate the resonance frequencies. The results of this study can be utilized in the development of NEMS and MEMS, which play a vital role in numerous sectors, such as telecommunications, automotive, and biomedical devices. By optimizing the resonance characteristics of nanoplates, the performance of these systems can be enhanced.

2. Numerical modeling of the problem

The object of study in this research (Fig. 1) is a rectangular nanoplate made of a piezoelectric polymer. The rectangular nanoplate made of a piezoelectric polymer has specific dimensions for its length a , width b , and thickness h , and is positioned on the Pasternak foundation. All boundary conditions are assumed to be supported simply. In addition, the nanoplate experiences biaxial forces, a nanoparticle moving in a circular trajectory, and an electric field $\hat{\Phi}(x, y, z, t)$.

2.1. Non-local constitutive relations of piezoelectric materials

Smart materials are an innovative class of materials recently introduced to the industrial sector. The application of electrical excitation can induce deformation in intelligent materials. In the realm of intelligent materials, piezoelectric materials predominate. Piezoelectric materials undergo electrical polarization and generate an electrical potential in response to mechanical loading; conversely, they exhibit mechanical strains when exposed to an electric field. Literature acknowledges the widespread application of these materials as sensors and actuators in the automotive, aerospace, computer, medical, and home

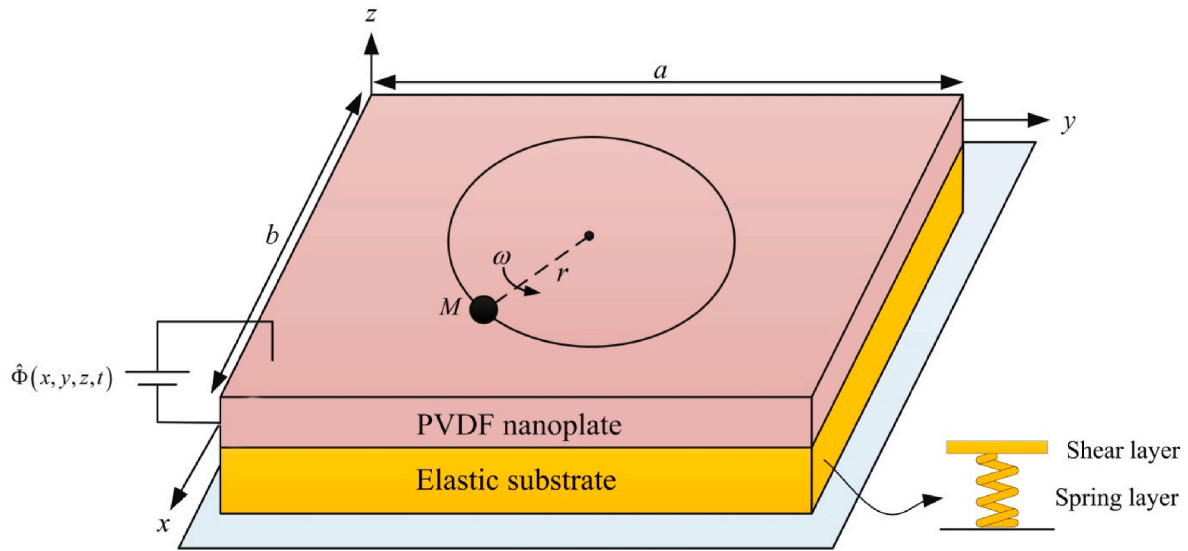


Fig. 1. Geometric configuration of the PVDF nanoplate carrying an orbiting nanoparticle.

appliance industries [30]. The intelligent polyvinylidene fluoride polymer possesses piezoelectric properties. It is non-combustible and possesses distinctive characteristics, including chemical, thermal, and electrical stability, as well as low dielectric constants [31]. The constituent relationships of PVDF materials for strain and mechanical stress, in addition to field strength and electrostatic flux density, are delineated as follows [32,33]:

$$\begin{Bmatrix} \sigma_{xx} \\ \sigma_{yy} \\ \tau_{yz} \\ \tau_{zx} \\ \tau_{xy} \end{Bmatrix} = \begin{bmatrix} C_{11} & C_{12} & 0 & 0 & 0 \\ C_{21} & C_{22} & 0 & 0 & 0 \\ 0 & 0 & C_{44} & 0 & 0 \\ 0 & 0 & 0 & C_{55} & 0 \\ 0 & 0 & 0 & 0 & C_{66} \end{bmatrix} \begin{Bmatrix} \varepsilon_{xx} \\ \varepsilon_{yy} \\ \gamma_{yz} \\ \gamma_{zx} \\ \gamma_{xy} \end{Bmatrix} - \begin{bmatrix} 0 & 0 & e_{31} \\ 0 & 0 & e_{32} \\ 0 & e_{24} & 0 \\ e_{15} & 0 & 0 \\ 0 & 0 & 0 \end{bmatrix} \begin{Bmatrix} E_{xx} \\ E_{yy} \\ E_{zz} \end{Bmatrix}, \quad (1)$$

$$\begin{Bmatrix} D_{xx} \\ D_{yy} \\ D_{zz} \end{Bmatrix} = \begin{bmatrix} 0 & 0 & 0 & e_{15} & 0 \\ 0 & 0 & e_{24} & 0 & 0 \\ e_{31} & e_{32} & 0 & 0 & 0 \end{bmatrix} \begin{Bmatrix} \varepsilon_{xx} \\ \varepsilon_{yy} \\ \gamma_{yz} \\ \gamma_{zx} \\ \gamma_{xy} \end{Bmatrix} + \begin{bmatrix} \in_{11} & 0 & 0 \\ 0 & \in_{22} & 0 \\ 0 & 0 & \in_{33} \end{bmatrix} \begin{Bmatrix} E_{xx} \\ E_{yy} \\ E_{zz} \end{Bmatrix}, \quad (2)$$

where C_{ij} , \in_{ij} , and e_{ij} represent the elastic, dielectric, and piezoelectric coefficients, respectively. Also, the electric fields $E_i (i = x, y, z)$ can be obtained as functions of electric potential $\hat{\Phi}(x, y, z, t)$ as follows [34]:

$$E = -\nabla \hat{\Phi}(x, y, z, t). \quad (3)$$

where ∇ is the gradient operator. The representation of the electric potential distribution along the thickness direction can be expressed as follows [35] using the Maxwell equation:

$$\hat{\Phi}(x, y, z, t) = -\cos\left(\frac{\pi z}{h}\right)\Phi(x, y, t) + \frac{2zV_0}{h}, \quad (4)$$

where $\Phi(x, y, t)$ denotes the electric potential distribution caused by bending in the mid-surface of the PVDF nanoplate and V_0 stands for the external electric voltage.

Eringen's non-local theory [36,37] can also be utilized for

piezoelectric materials. The non-local constitutive relations for piezoelectric polymeric materials are formulated by utilizing the differential version of this theory and Eqs. (1) and (2) as follows:

$$\begin{Bmatrix} \sigma_{xx} \\ \sigma_{yy} \\ \tau_{yz} \\ \tau_{zx} \\ \tau_{xy} \end{Bmatrix} - \mu \nabla^2 \begin{Bmatrix} \sigma_{xx} \\ \sigma_{yy} \\ \tau_{yz} \\ \tau_{zx} \\ \tau_{xy} \end{Bmatrix} = \begin{bmatrix} C_{11} & C_{12} & 0 & 0 & 0 \\ C_{21} & C_{22} & 0 & 0 & 0 \\ 0 & 0 & C_{44} & 0 & 0 \\ 0 & 0 & 0 & C_{55} & 0 \\ 0 & 0 & 0 & 0 & C_{66} \end{bmatrix} \begin{Bmatrix} \varepsilon_{xx} \\ \varepsilon_{yy} \\ \gamma_{yz} \\ \gamma_{zx} \\ \gamma_{xy} \end{Bmatrix} - \begin{bmatrix} 0 & 0 & e_{31} \\ 0 & 0 & e_{32} \\ 0 & e_{24} & 0 \\ e_{15} & 0 & 0 \\ 0 & 0 & 0 \end{bmatrix} \begin{Bmatrix} E_{xx} \\ E_{yy} \\ E_{zz} \end{Bmatrix}, \quad (5)$$

$$\begin{Bmatrix} D_{xx} \\ D_{yy} \\ D_{zz} \end{Bmatrix} - \mu \nabla^2 \begin{Bmatrix} D_{xx} \\ D_{yy} \\ D_{zz} \end{Bmatrix} = \begin{bmatrix} 0 & 0 & 0 & e_{15} & 0 \\ 0 & 0 & e_{24} & 0 & 0 \\ e_{31} & e_{32} & 0 & 0 & 0 \end{bmatrix} \begin{Bmatrix} \varepsilon_{xx} \\ \varepsilon_{yy} \\ \gamma_{yz} \\ \gamma_{zx} \\ \gamma_{xy} \end{Bmatrix} + \begin{bmatrix} \in_{11} & 0 & 0 \\ 0 & \in_{22} & 0 \\ 0 & 0 & \in_{33} \end{bmatrix} \begin{Bmatrix} E_{xx} \\ E_{yy} \\ E_{zz} \end{Bmatrix}, \quad (6)$$

where ∇^2 is the Laplacian operator, and $\mu = (e_0 a)^2$ is the non-local parameter. Setting $\mu = 0$ reduces the non-local stress and flux density in Eqs. (5) and (6) to local ones.

2.2. Governing equations of motion

The displacements in the x, y, and z directions, as per Mindlin's plate theory, are denoted as follows, respectively [38,39]:

$$\begin{aligned} u_1(x, y, z, t) &= z\psi_x(x, y, t), \\ u_2(x, y, z, t) &= z\psi_y(x, y, t), \\ u_3(x, y, z, t) &= w(x, y, t), \end{aligned} \quad (7)$$

where $w(x, y, t)$ is the nanoplate mid-surface transverse displacement, and ψ_x and ψ_y are the rotation functions of straight lines perpendicular to the nanoplate mid-surface. The normal strains (ε_{xx} , ε_{yy} , ε_{zz}) and shear strains (γ_{xy} , γ_{xz} , γ_{yz}) are determined as follows by taking into account strain-displacement relations associated with small deformation of the nanoplate [40,41]:

$$\epsilon_{xx} = z \frac{\partial \psi_x}{\partial x}, \epsilon_{yy} = z \frac{\partial \psi_y}{\partial y}, \epsilon_{zz} = 0,$$

$$\gamma_{xy} = z \left(\frac{\partial \psi_x}{\partial y} + \frac{\partial \psi_y}{\partial x} \right), \gamma_{xz} = \psi_x + \frac{\partial w}{\partial x}, \gamma_{yz} = \psi_y + \frac{\partial w}{\partial y}. \quad (8)$$

The PVDF nanoplate's strain energy is written as [42]:

$$U = \frac{1}{2} \int_V \left(\sigma_{xx} \epsilon_{xx} + \sigma_{yy} \epsilon_{yy} + \tau_{yz} \gamma_{yz} + \tau_{zx} \gamma_{zx} + \tau_{xy} \gamma_{xy} - D_{xx} E_{xx} - D_{yy} E_{yy} - D_{zz} E_{zz} \right) dV. \quad (9)$$

By inserting Eq. (8) into Eq. (9) and performing integration throughout the thickness of the PVDF nanoplate, the resultant equation is derived:

$$U = \frac{1}{2} \int_A \left[M_{xx} \frac{\partial \psi_x}{\partial x} + M_{yy} \frac{\partial \psi_y}{\partial y} + M_{xy} \left(\frac{\partial \psi_x}{\partial y} + \frac{\partial \psi_y}{\partial x} \right) + Q_{xz} \left(\frac{\partial w}{\partial x} + \psi_x \right) + Q_{yz} \left(\frac{\partial w}{\partial y} + \psi_y \right) \right] dA - \frac{1}{2} \int_V \left[D_x \left(\cos \left(\frac{\pi z}{h} \right) \frac{\partial \Phi}{\partial x} \right) + D_y \left(\cos \left(\frac{\pi z}{h} \right) \frac{\partial \Phi}{\partial y} \right) - D_z \left(\frac{\pi}{h} \sin \left(\frac{\pi z}{h} \right) \Phi + \frac{2V_0}{h} \right) \right] dV, \quad (10)$$

in which

$$\{M_{xx}, M_{yy}, M_{xy}\} = \int_{-h/2}^{h/2} \{\sigma_{xx}, \sigma_{yy}, \sigma_{xy}\} z dz, \{Q_{xz}, Q_{yz}\} = \kappa \int_{-h/2}^{h/2} \{\tau_{xz}, \tau_{yz}\} dz, \quad (11)$$

where M_{xx} , M_{yy} , and M_{xy} are bending moments, Q_{xz} and Q_{yz} represent resultant shear forces, and κ is the shear correction factor. The mathematical representation of the work performed by the electrical voltage, biaxial loading, elastic foundation, and moving nanoparticle is as follows [43,44]:

$$V = \frac{1}{2} \int_A \left[(N_x + 2e_{31} V_0) \left(\frac{\partial w}{\partial x} \right)^2 + (N_y + 2e_{32} V_0) \left(\frac{\partial w}{\partial y} \right)^2 - (k_w w - k_g \nabla^2 w) w + q(x, y, t) w \right] dA, \quad (12)$$

where N_x and N_y are in-plane applied loads along x and y directions, respectively, and k_g and k_w are Pasternak and Winkler foundation modules. Furthermore, $q(x, y, t)$ implies the transverse force due to the nanoparticle movement over the PVDF nanoplate. By considering inertial effects of the nanoparticle, $q(x, y, t)$ can be stated as follows [45,46]:

$$q(x, y, t) = -M \left(-g + \ddot{w} + \frac{\partial^2 w}{\partial x^2} \dot{x}^2 + \frac{\partial^2 w}{\partial y^2} \dot{y}^2 + 2 \frac{\partial^2 w}{\partial x \partial y} \dot{x} \dot{y} + 2 \frac{\partial^2 w}{\partial x \partial t} \dot{x} + 2 \frac{\partial^2 w}{\partial y \partial t} \dot{y} + \frac{\partial w}{\partial x} \ddot{x} + \frac{\partial w}{\partial y} \ddot{y} \right) \bar{\delta}(x - x_m(t)) \bar{\delta}(y - y_m(t)), \quad (13)$$

where g and $\bar{\delta}(\cdot)$ denote the gravity acceleration and delta-Dirac function, respectively. The expression for the position of the nanoparticle, which is orbiting the center of the PVDF nanoplate along a circular path of radius r and angular velocity ω , is as follows:

$$x_M(t) = \frac{a}{2} + r \cos(\omega t), y_M(t) = \frac{b}{2} + r \sin(\omega t). \quad (14)$$

The kinetic energy of the PVDF nanoplate is expressed as follows [47]:

$$K = \frac{\rho}{2} \int_V \left(\left(\frac{\partial u_1}{\partial t} \right)^2 + \left(\frac{\partial u_2}{\partial t} \right)^2 + \left(\frac{\partial u_3}{\partial t} \right)^2 \right) dV, \quad (15)$$

where ρ denotes the density of PVDF nanoplate. By substituting displacements u_1 , u_2 , and u_3 from Eq. (7) into Eq. (15), the kinetic energy

can be determined using the subsequent formula:

$$K = \frac{\rho h}{2} \int_A \left(\left(\frac{\partial w}{\partial t} \right)^2 - \frac{h^2}{12} \left\{ \left(\frac{\partial \psi_x}{\partial t} \right)^2 + \left(\frac{\partial \psi_y}{\partial t} \right)^2 \right\} \right) dA. \quad (16)$$

The following is how Hamilton's principle is applied to derive the motion equations [48,49]:

$$\int_0^t \delta(U + V - K) dt = 0, \quad (17)$$

where δ implies the variational operator. By substituting Eqs. (10), (12) and (16) into Eq. (17), we can get the local equations that govern the PVDF nanoplate under biaxial loading, when it is activated by a moving

nanoparticle and electric field.

$$\frac{\partial Q_{xz}}{\partial x} + \frac{\partial Q_{yz}}{\partial y} - k_w w + k_g \nabla^2 w + (N_{xm} + N_{xe}) \frac{\partial^2 w}{\partial x^2} + (N_{ym} + N_{ye}) \frac{\partial^2 w}{\partial y^2} - \rho h \frac{\partial^2 w}{\partial t^2} + q(x, y, t) = 0, \quad (18)$$

$$\frac{\partial M_{xx}}{\partial x} + \frac{\partial M_{xy}}{\partial y} - Q_{xz} - \frac{\rho h^3}{12} \frac{\partial^2 \psi_x}{\partial t^2} = 0, \quad (19)$$

$$\frac{\partial M_{yy}}{\partial y} + \frac{\partial M_{xy}}{\partial x} - Q_{yz} - \frac{\rho h^3}{12} \frac{\partial^2 \psi_y}{\partial t^2} = 0, \quad (20)$$

$$\int_{-h/2}^{h/2} \left[\cos\left(\frac{\pi z}{h}\right) \frac{\partial D_{xx}}{\partial x} + \cos\left(\frac{\pi z}{h}\right) \frac{\partial D_{yy}}{\partial y} + \frac{\pi}{h} \sin\left(\frac{\pi z}{h}\right) D_{zz} \right] dz = 0. \quad (21)$$

By using Eqs. (5), (6) and (11), and (18–21), the governing non-local equations for the transverse vibration of the PVDF nanoplate can be obtained in terms of w , ψ_x , ψ_y , and Φ as follows:

$$\begin{aligned} & \kappa h \left(C_{55} \frac{\partial \psi_x}{\partial x} + C_{55} \frac{\partial^2 w}{\partial x^2} + C_{44} \frac{\partial \psi_y}{\partial y} + C_{44} \frac{\partial^2 w}{\partial y^2} \right) - \frac{2\kappa}{\beta} \left(e_{15} \frac{\partial^2 \Phi}{\partial x^2} + e_{24} \frac{\partial^2 \Phi}{\partial y^2} \right) \\ & - (1 - \mu \nabla^2) \left[k_w w - k_g \nabla^2 w - (N_x + 2e_{31} V_0) \frac{\partial^2 w}{\partial x^2} - (N_y + 2e_{32} V_0) \frac{\partial^2 w}{\partial y^2} + \rho h \frac{\partial^2 w}{\partial t^2} \right. \\ & \left. + M \left(-g + \ddot{w} + \frac{\partial^2 w}{\partial x^2} \dot{x}^2 + \frac{\partial^2 w}{\partial y^2} \dot{y}^2 + 2 \frac{\partial^2 w}{\partial x \partial y} \dot{x} \dot{y} + 2 \frac{\partial^2 w}{\partial x \partial t} \dot{x} + 2 \frac{\partial^2 w}{\partial y \partial t} \dot{y} + \frac{\partial w}{\partial x} \ddot{x} + \frac{\partial w}{\partial y} \ddot{y} \right) \bar{\delta}(x - x_M(t)) \bar{\delta}(y - y_M(t)) \right] = 0, \end{aligned} \quad (22)$$

$$\begin{Bmatrix} w(x, y, t) \\ \psi_x(x, y, t) \\ \psi_y(x, y, t) \\ \Phi(x, y, t) \end{Bmatrix} = \sum_{m=1}^{\infty} \sum_{n=1}^{\infty} \begin{Bmatrix} W_{mn}(t) \sin\left(\frac{m\pi x}{a}\right) \sin\left(\frac{n\pi y}{b}\right) \\ \psi_{xmn}(t) \cos\left(\frac{m\pi x}{a}\right) \sin\left(\frac{n\pi y}{b}\right) \\ \psi_{ymn}(t) \sin\left(\frac{m\pi x}{a}\right) \cos\left(\frac{n\pi y}{b}\right) \\ \Phi_{mn}(t) \sin\left(\frac{m\pi x}{a}\right) \sin\left(\frac{n\pi y}{b}\right) \end{Bmatrix}, \quad (26)$$

where $W_{mn}(t)$, $\psi_{xmn}(t)$, $\psi_{ymn}(t)$, and $\Phi_{mn}(t)$ are unknown coefficients,

and m and n indicate mode numbers along x and y directions, respectively. By substituting Eq. (26) into Eqs. 22–25 and using the Galerkin procedure, the following coupled time-varying ODEs are obtained for $(m, n) = (1, 1)$:

$$\begin{aligned} & \left(\begin{bmatrix} M_{11} & 0 & 0 & 0 \\ 0 & M_{22} & 0 & 0 \\ 0 & 0 & M_{33} & 0 \\ 0 & 0 & 0 & 0 \end{bmatrix} + \begin{bmatrix} \bar{M}_{11}(t) & 0 & 0 & 0 \\ 0 & 0 & 0 & 0 \\ 0 & 0 & 0 & 0 \\ 0 & 0 & 0 & 0 \end{bmatrix} \right) \begin{Bmatrix} \dot{W}_{11} \\ \dot{\psi}_{x11} \\ \dot{\psi}_{y11} \\ \dot{\Phi}_{11} \end{Bmatrix} + \begin{bmatrix} \bar{C}_{11}(t) & 0 & 0 & 0 \\ 0 & 0 & 0 & 0 \\ 0 & 0 & 0 & 0 \\ 0 & 0 & 0 & 0 \end{bmatrix} \begin{Bmatrix} \dot{W}_{11} \\ \dot{\psi}_{x11} \\ \dot{\psi}_{y11} \\ \dot{\Phi}_{11} \end{Bmatrix} + \begin{bmatrix} K_{11} & K_{12} & K_{13} & K_{14} \\ K_{21} & K_{22} & K_{23} & K_{24} \\ K_{31} & K_{32} & K_{33} & K_{34} \\ K_{41} & K_{42} & K_{43} & K_{44} \end{bmatrix} \\ & + \begin{bmatrix} \bar{K}_{11}(t) & 0 & 0 & 0 \\ 0 & 0 & 0 & 0 \\ 0 & 0 & 0 & 0 \\ 0 & 0 & 0 & 0 \end{bmatrix} \begin{Bmatrix} W_{11} \\ \psi_{x11} \\ \psi_{y11} \\ \Phi_{11} \end{Bmatrix} = \begin{Bmatrix} \bar{F}_1(t) \\ 0 \\ 0 \\ 0 \end{Bmatrix}, \end{aligned} \quad (27)$$

$$\begin{aligned} & \frac{h^3}{12} \left(C_{11} \frac{\partial^2 \psi_x}{\partial x^2} + C_{12} \frac{\partial^2 \psi_y}{\partial x \partial y} + C_{66} \left(\frac{\partial^2 \psi_x}{\partial y^2} + \frac{\partial^2 \psi_y}{\partial x \partial y} \right) \right) \\ & - \kappa h \left(C_{55} \psi_x + C_{55} \frac{\partial w}{\partial x} \right) + \frac{2}{\beta} \left(e_{31} \frac{\partial \Phi}{\partial x} + \kappa e_{15} \frac{\partial \Phi}{\partial x} \right) - (1 - \mu \nabla^2) I_2 \frac{\partial^2 \psi_x}{\partial t^2} = 0, \end{aligned} \quad (23)$$

$$\begin{aligned} & \frac{h^3}{12} \left(C_{11} \frac{\partial^2 \psi_y}{\partial y^2} + C_{12} \frac{\partial^2 \psi_x}{\partial x \partial y} + C_{66} \left(\frac{\partial^2 \psi_y}{\partial x^2} + \frac{\partial^2 \psi_x}{\partial x \partial y} \right) \right) \\ & - \kappa h \left(C_{44} \psi_y + C_{44} \frac{\partial w}{\partial y} \right) + \frac{2}{\beta} \left(e_{32} \frac{\partial \Phi}{\partial y} + \kappa e_{24} \frac{\partial \Phi}{\partial y} \right) - (1 - \mu \nabla^2) I_2 \frac{\partial^2 \psi_y}{\partial t^2} = 0, \end{aligned} \quad (24)$$

$$\begin{aligned} & \frac{2h}{\pi} \left(e_{15} \frac{\partial \psi_x}{\partial x} + e_{31} \frac{\partial \psi_x}{\partial x} + e_{15} \frac{\partial^2 w}{\partial x^2} + e_{24} \frac{\partial \psi_y}{\partial y} + e_{32} \frac{\partial \psi_y}{\partial y} + e_{24} \frac{\partial^2 w}{\partial y^2} \right) \\ & + \frac{1}{2} \left(\epsilon_{11} h \frac{\partial^2 \Phi}{\partial x^2} + \epsilon_{22} h \frac{\partial^2 \Phi}{\partial y^2} - \epsilon_{33} \pi^2 \Phi \right) = 0. \end{aligned} \quad (25)$$

3. Solution procedure

The assumptions regarding the displacement components are as follows [50,51]:

The components of the above matrices are presented in Appendix A. To enhance readability, Equation (27) is converted to its dimensionless counterpart in Appendix B.

4. Incremental harmonic balance method

The incremental harmonic balance method is a semi-analytical technique that can be implemented on a computer. By substituting finite Fourier series for the periodic response of a dynamic equation, this approach converts the equations into a system of incremental linear algebraic equations. Following the application of the Galerkin technique to these algebraic equations, the periodic response of the system is determined iteratively. The approach demonstrates the ability to efficiently resolve both weak and strong nonlinear systems in addition to linear ones. The IHB method offers more precise solutions across a significantly broader range of parameters in comparison to numerical approaches like the energy-rate method and Floquet theory, due to its ability to account for multiple harmonics. A detailed explanation of how to calculate resonance frequencies using this method is provided below. The governing Eq. (B.2) includes terms such as $\sin(\pi\zeta \cos(\tau))$, $\sin(\pi\eta \sin(\tau))$, $\cos(\pi\eta \sin(\tau))$, and $\cos(\pi\zeta \cos(\tau))$. To avoid certain difficulties in the IHB procedure, the following terms have been replaced by

their Fourier series [52]:

$$\begin{aligned} \cos(\pi\zeta \cos(\tau)) &= J_0(\pi\zeta) + 2 \sum_{i=1}^{\infty} (-1)^i J_{2i}(\pi\zeta) \cos(2i\tau), \\ \cos(\pi\eta \sin(\tau)) &= J_0(\pi\eta) + 2 \sum_{i=1}^{\infty} J_{2i}(\pi\eta) \cos(2i\tau), \\ \sin(\pi\zeta \cos(\tau)) &= 2 \sum_{i=0}^{\infty} (-1)^i J_{2i+1}(\pi\zeta) \cos((2i+1)\tau), \\ \sin(\pi\eta \sin(\tau)) &= 2 \sum_{i=0}^{\infty} J_{2i+1}(\pi\eta) \sin((2i+1)\tau), \end{aligned} \tag{28}$$

where $J_s(x)$ $s = 1, 2, \dots$ is the Bessel function of the first kind. If $\mathbf{Q}^*(\tau) = \{\tilde{W}_{11}^*, \tilde{\psi}_{x11}^*, \tilde{\psi}_{y11}^*, \tilde{\Phi}_{11}^*\}^T$ represents the current vibrational state for the excitation parameters α^* and Ω^* , then the following equations can be used to derive the neighboring state:

$$\mathbf{Q}(\tau) = \mathbf{Q}^*(\tau) + \Delta\mathbf{Q}(\tau), \alpha = \alpha^* + \Delta\alpha, \Omega = \Omega^* + \Delta\Omega, \tag{29}$$

where $\Delta\mathbf{Q}(\tau)$, $\Delta\alpha$, and $\Delta\Omega$ stand for small increments. By inserting Equation (29) into the homogeneous version of Equation (B.2) and disregarding the negligible incremental nonlinear terms, we obtain:

$$\begin{aligned} \Omega^{*2} (\mathbf{M}_1 + \alpha^* \mathbf{M}_2(\tau)) \Delta\mathbf{Q}'' + \alpha^* \Omega^{*2} \mathbf{C}_1(\tau) \Delta\mathbf{Q}' + (\mathbf{K}_1 + \alpha^* \Omega^{*2} \mathbf{K}_2(\tau)) \Delta\mathbf{Q} \\ = \mathbf{R} - \left\{ \Omega^{*2} (\mathbf{M}_2(\tau) \mathbf{Q}^{*''} + \mathbf{C}_1(\tau) \mathbf{Q}^{*'} + \mathbf{K}_2(\tau) \mathbf{Q}^*) \right\} \Delta\alpha \\ - \{ 2\Omega^* ((\mathbf{M}_1 + \alpha^* \mathbf{M}_2(\tau)) \mathbf{Q}^{*''} + \alpha^* \mathbf{C}_1(\tau) \mathbf{Q}^{*'} + \alpha^* \mathbf{K}_2(\tau) \mathbf{Q}^*) \} \Delta\Omega, \end{aligned} \tag{30}$$

where

$$\begin{aligned} \mathbf{M}_1 = \begin{bmatrix} \tilde{M}_{11} & 0 & 0 & 0 \\ 0 & \tilde{M}_{22} & 0 & 0 \\ 0 & 0 & \tilde{M}_{33} & 0 \\ 0 & 0 & 0 & 0 \end{bmatrix}, \mathbf{M}_2 = \begin{bmatrix} \tilde{M}_{11}(\tau) & 0 & 0 & 0 \\ 0 & 0 & 0 & 0 \\ 0 & 0 & 0 & 0 \\ 0 & 0 & 0 & 0 \end{bmatrix}, \mathbf{C}_1 = \begin{bmatrix} \tilde{C}_{11}(\tau) & 0 & 0 & 0 \\ 0 & 0 & 0 & 0 \\ 0 & 0 & 0 & 0 \\ 0 & 0 & 0 & 0 \end{bmatrix}, \\ \mathbf{K}_1 = \begin{bmatrix} \tilde{K}_{11} & \tilde{K}_{12} & \tilde{K}_{13} & \tilde{K}_{14} \\ \tilde{K}_{21} & \tilde{K}_{22} & \tilde{K}_{23} & \tilde{K}_{24} \\ \tilde{K}_{31} & \tilde{K}_{32} & \tilde{K}_{33} & \tilde{K}_{34} \\ \tilde{K}_{41} & \tilde{K}_{42} & \tilde{K}_{43} & \tilde{K}_{44} \end{bmatrix}, \mathbf{K}_2 = \begin{bmatrix} \tilde{K}_{11}(\tau) & 0 & 0 & 0 \\ 0 & 0 & 0 & 0 \\ 0 & 0 & 0 & 0 \\ 0 & 0 & 0 & 0 \end{bmatrix}, \end{aligned} \tag{31}$$

$$\mathbf{R} = -\Omega^{*2} (\mathbf{M}_1 + \alpha^* \mathbf{M}_2(\tau)) \mathbf{Q}^{*''} - \alpha^* \Omega^{*2} \mathbf{C}_1(\tau) \mathbf{Q}^{*'} - (\mathbf{K}_1 + \alpha^* \Omega^{*2} \mathbf{K}_2(\tau)) \mathbf{Q}^*.$$

In the given equation, \mathbf{R} denotes the residual, which attains a value of zero when Ω^* is a precise solution. Resonance occurs in linear time-varying systems when the excitation frequency on the right-hand side of the governing equation matches the periodic response frequency. Hence, the residual term is employed to control the precision of the solution. By substituting Equation (28) into Equation (B.2), it becomes evident that the right-hand side of Equation (B.2) consists of cosine terms with frequencies that are even. Thus, the harmonic response mentioned in the equation is considered while calculating the resonance frequencies for the homogeneous equation [47]:

$$\begin{aligned} \mathbf{Q}^*(\tau) &= \sum_{i=2,4,6,\dots}^N b_i \cos(i\tau) = \mathbf{T} \mathbf{a}_{j,i}, j = 1, 2, 3, 4, \\ \Delta\mathbf{Q}^*(\tau) &= \sum_{i=2,4,6,\dots}^N \Delta b_i \cos(i\tau) = \mathbf{T} \Delta \mathbf{a}_{j,i}, j = 1, 2, 3, 4, \end{aligned} \tag{32}$$

where

$$\begin{aligned} \mathbf{T} &= \{\cos(2\tau), \cos(4\tau), \cos(6\tau), \dots\}, \mathbf{a}_{j,i} = \{a_{j2}, a_{j4}, a_{j6}, \dots\}^T, \\ \Delta \mathbf{a}_{j,i} &= \{\Delta a_{j2}, \Delta a_{j4}, \Delta a_{j6}, \dots\}^T. \end{aligned} \tag{33}$$

Therefore \mathbf{Q}^* , and $\Delta\mathbf{Q}$ can be written as:

$$\mathbf{Q}^* = \mathbf{Y} \mathbf{A}, \Delta\mathbf{Q} = \mathbf{Y} \Delta \mathbf{A}, \tag{34}$$

where

$$\mathbf{Y} = \begin{bmatrix} \mathbf{T} & 0 & 0 & 0 \\ 0 & \mathbf{T} & 0 & 0 \\ 0 & 0 & \mathbf{T} & 0 \\ 0 & 0 & 0 & \mathbf{T} \end{bmatrix}, \mathbf{A} = \begin{Bmatrix} \mathbf{a}_1 \\ \mathbf{a}_2 \\ \mathbf{a}_3 \\ \mathbf{a}_4 \end{Bmatrix}, \Delta \mathbf{A} = \begin{Bmatrix} \Delta \mathbf{a}_1 \\ \Delta \mathbf{a}_2 \\ \Delta \mathbf{a}_3 \\ \Delta \mathbf{a}_4 \end{Bmatrix}. \tag{35}$$

Applying the Galerkin method to Eq. (30) over a specific time interval yields the subsequent equation:

$$\begin{aligned} & \int_0^\pi \delta(\Delta \mathbf{Q})^T \left[\Omega^{*2} (\mathbf{M}_1 + \alpha^* \mathbf{M}_2(\tau)) \Delta \mathbf{Q}'' + \alpha^* \Omega^{*2} \mathbf{C}_1(\tau) \Delta \mathbf{Q}' + (\mathbf{K}_1 + \alpha^* \Omega^{*2} \mathbf{K}_2(\tau)) \Delta \mathbf{Q} \right] d\tau \\ & = \int_0^\pi \delta(\Delta \mathbf{Q})^T \left[\mathbf{R} - \left\{ \Omega^{*2} (\mathbf{M}_2(\tau) \mathbf{Q}^{*''} + \mathbf{C}_1(\tau) \mathbf{Q}^{*' +} + \mathbf{K}_2(\tau) \mathbf{Q}^*) \right\} \Delta \alpha \right. \\ & \left. - \{ 2\Omega^* ((\mathbf{M}_1 + \alpha^* \mathbf{M}_2(\tau)) \mathbf{Q}^{*''} + \alpha^* \mathbf{C}_1(\tau) \mathbf{Q}^{*' +} + \alpha^* \mathbf{K}_2(\tau) \mathbf{Q}^*) \} \Delta \Omega \right] d\tau, \end{aligned} \quad (36)$$

Then, substituting Eq. (34) into Eq. (36) leads to a set of algebraic linear equations with parameters $\Delta \mathbf{A}$, $\Delta \alpha$, and $\Delta \Omega$ as follows:

$$\mathbf{S}_{\Delta \mathbf{A}} \Delta \mathbf{A} + \mathbf{S}_{\Delta \alpha} \Delta \alpha + \mathbf{S}_{\Delta \Omega} \Delta \Omega = \mathbf{R}, \quad (37)$$

where

$$\begin{aligned} \mathbf{S}_{\Delta \mathbf{A}} &= \int_0^\pi \mathbf{Y}^T \left[\Omega^{*2} (\mathbf{M}_1 + \alpha^* \mathbf{M}_2(\tau)) \mathbf{Y}'' + \alpha^* \Omega^{*2} \mathbf{C}_1(\tau) \mathbf{Y}' + (\mathbf{K}_1 + \alpha^* \Omega^{*2} \mathbf{K}_2(\tau)) \mathbf{Y} \right] d\tau, \\ \mathbf{S}_{\Delta \alpha} &= \int_0^\pi \mathbf{Y}^T \left[\Omega^{*2} (\mathbf{M}_2(\tau) \mathbf{Y}'' + \mathbf{C}_1 \mathbf{Y}' + 2 \mathbf{K}_2(\tau) \mathbf{Y}) \right] \mathbf{A} d\tau, \\ \mathbf{S}_{\Delta \Omega} &= \int_0^\pi \mathbf{Y}^T [2\Omega^* ((\mathbf{M}_1 + \alpha^* \mathbf{M}_2(\tau)) \mathbf{Y}'' + \alpha^* \mathbf{C}_1(\tau) \mathbf{Y}' + \alpha^* \mathbf{K}_2(\tau) \mathbf{Y})] \mathbf{A} d\tau, \\ \mathbf{R} &= - \int_0^\pi \mathbf{Y}^T \left[\Omega^{*2} (\mathbf{M}_1 + \alpha^* \mathbf{M}_2(\tau)) \mathbf{Y}'' + \alpha^* \Omega^{*2} \mathbf{C}_1(\tau) \mathbf{Y}' + (\mathbf{K}_1 + \alpha^* \Omega^{*2} \mathbf{K}_2(\tau)) \mathbf{Y} \right] \mathbf{A} d\tau. \end{aligned} \quad (38)$$

Equation (37) is utilized to compute resonance frequencies based on the provided parameters \mathbf{A} , α^* , and Ω^* . Due to the nonlinearity of this equation for these quantities, it is not directly solvable. Instead, a linear equation involving $\Delta \mathbf{A}$, $\Delta \alpha$, and $\Delta \Omega$ is solved using a recursive algorithm, resulting in the calculation of dimensionless resonance frequencies. The recursive algorithm is further elucidated in Ref. [47].

5. Results and discussion

By considering solely the initial summation component of the harmonic response, as specified in Eq. (22), the resonance curve associated with the initial excitation frequency can be obtained. For the values on this curve, the amplitude of the vibrations of the PVDF nanoplate will increase with time. By including additional harmonic elements of summation, distinct resonance curves can be generated. The resonance curves of the initial four excitation frequencies in the α - Ω plane for a square PVDF nanoplate of uniform thickness $h = 2\text{nm}$, length $a = 40\text{nm}$, and width $b = 40\text{nm}$, as well as the mechanical parameters specified in Table 1, are illustrated in Fig. 2. Validating the resonance curves requires the application of the fourth-order Runge-Kutta method to solve the governing equations. Fig. S1 in the supplementary information (SI) illustrates the frequency spectrum and time history of the system for parameters selected from the initial, secondary, and tertiary resonance curves. Evidently, at these values, the amplitude of the

oscillations within the system continues to increase, potentially leading to the failure of the nanostructure. In addition, the concurrence of

response and excitation frequencies as depicted in the frequency spectrum diagrams provides additional evidence for the system's resonance.

A comparative analysis is conducted to examine the precision of the methodology implemented (see Fig. S2 in SI). To accomplish this, the piezoelectric coefficients, non-local effect, biaxial forces, and elastic medium are disregarded, while Rofooei and Nikkhoo's research [53] is utilized to modify the mechanical properties and geometric dimensions.

Following this, the second resonance curve linked to the macroscopic plate housing the orbiting mass is presented, in conjunction with the results reported in Ref. [53], which utilizes the eigenfunction expansion method. The congruence between the present findings and the results reported in the literature serves to underscore the soundness of the present analysis.

This study investigates the impact of different variables on the resonance frequencies that are linked to the initial excitation frequency.

Table 1

Piezoelectric, elastic, and dielectric coefficients of PVDF material [54].

e_{31}	$= -0.13$	C/m^2
e_{32}	$= -0.145$	C/m^2
e_{24}	$= -0.276$	C/m^2
e_{15}	$= -0.009$	C/m^2
e_{32}	$= -0.135$	C/m^2
C_{11}	$= 238.24$	GPa
C_{22}	$= 23.60$	GPa
C_{12}	$= 3.98$	GPa
C_{44}	$= 2.15$	GPa
C_{55}	$= 4.40$	GPa
C_{66}	$= 6.43$	GPa
ϵ_{11}/ϵ_0	$= 12.5$	
ϵ_{22}/ϵ_0	$= 11.98$	
ϵ_{33}/ϵ_0	$= 11.98$	
ϵ_0	$= 8.854185 \times 10^{-12}$	F/m

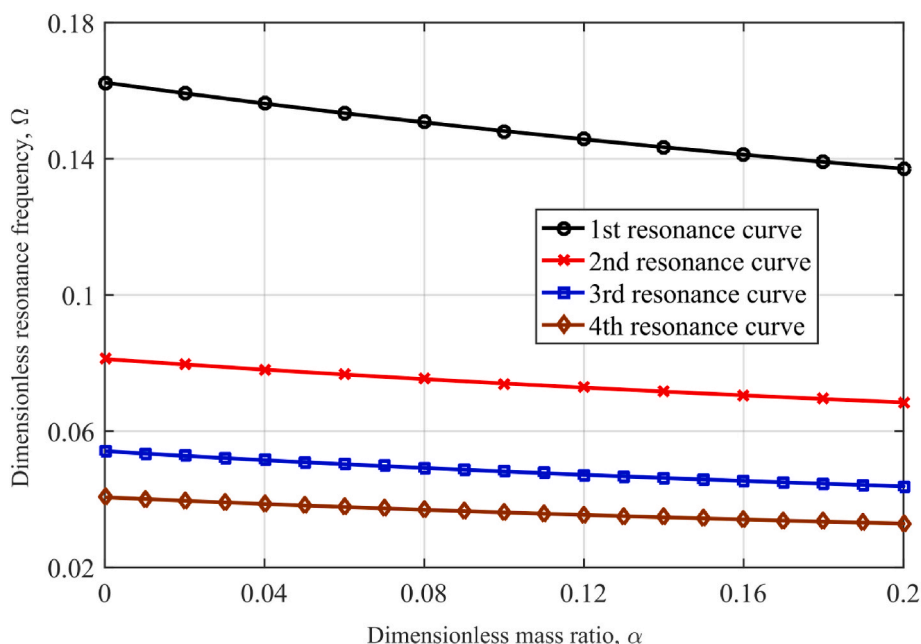


Fig. 2. Variation of dimensionless resonance frequency with dimensionless mass ratio; $a = b = 40$ nm, $h = 2$ nm, $\mu = 1$ nm², $\kappa = 5/6$, $r = 10$ nm, $V_0 = 1$ volt, $N_x = N_y = 0$, $k_w = 0$, $k_g = 0$.

The objective is to improve the resonance frequencies and provide an appropriate and precise blueprint for intelligent nanostructures. Consequently, Fig. 3 illustrates three-dimensional diagrams that depict the relationship between the dimensionless resonance frequency and the width and length of the nanoplate. The non-local parameter is represented by a variety of values. The dimensionless resonance frequencies increase as the width and length of the nanoplate decrease, as illustrated in Fig. 3. This can be attributed to the stiffer nanoplate. The non-local parameter is a measure of the influence of small-scale effects on the behavior of material. As the non-local parameter increases, the interaction forces between the atoms of the nanoplate diminish. This reduction in atomic interaction leads to a softening effect on the material, which is reflected in the decrease of resonance frequencies. Essentially, a higher non-local parameter indicates that the material behaves more like a continuum rather than a discrete structure, which can reduce its stiffness. On the other hand, a decrease in stiffness typically results in lower resonance frequencies.

Fig. 4 illustrates the effect of PVDF nanoplate thickness on dimensionless resonance frequencies for a range of non-local parameter values. It is indisputable that an augmentation in the thickness of the nanoplate will result in a substantial amplification of the resonance frequencies, owing to the nanoplate's rigidity.

The impact of excitation voltage on dimensionless resonance frequencies for different values of nanoplate thickness is illustrated in Fig. 5. An increase in voltage results in an enhancement of resonance frequencies. Additionally, the resonance frequencies of the PVDF nanoplate are greater when a negative voltage is applied than when a positive voltage is applied. This is because tensile and compressive tensions are induced in PVDF nanoplates, respectively, when positive and negative voltages are applied. Moreover, since the excitation voltage is applied in the direction of nanoplate thickness, as the nanoplate thickness increases, the resonance frequencies will be less affected. To gain a more comprehensive understanding of the impact of electrical voltage on resonance frequencies, the temporal response of the nanoplate at a dimensionless frequency of $\Omega = 0.177$ is illustrated in Fig. S3 in SI. An undesirable outcome can be avoided by stabilizing the dynamic response of the nanostructure through a small adjustment in the applied voltage, it has been discovered.

The relationship between the mass of the orbiting nanoparticle and

the dimensionless resonance frequencies for different values of the nanoplate's length and width is illustrated in Fig. 6. It is possible to deduce that as the mass of the nanoparticle increases, the resonance frequencies decrease. The variations of dimensionless resonance frequencies about the radius of nanoparticle motion for different values of non-local parameters are depicted in Fig. 7. The resonance frequencies increase in displacement from the center of the PVDF nanoplate as the nanoparticle progresses away from it.

For various values of non-local parameters, Fig. 8 illustrates three-dimensional graphs of dimensionless resonance frequencies with tensile axial force. The resonance frequencies of the system are positively influenced by the biaxial tensile forces; as the tensile force increases, the resonance frequencies ascend in value. This is because tensile stress induces stiffening in nanostructures.

The fluctuations in dimensionless resonance frequencies about non-local parameters are illustrated in Fig. 9(a) and (b), respectively, for various values of the Winkler constant k_w and the shear modulus k_g of the Pasternak foundation. The findings show that as the elastic constants of the substrate increase, the resonance frequencies rise. The parameter k_g is set to zero in Fig. 9(a). As a result, the elastic medium served as a Winkler foundation. The elastic environment is represented as a Pasternak foundation in Fig. 9(b) through the use of non-zero values for k_g and k_w . Upon comparing these figures, it becomes evident that the Winkler foundation exhibits lower resonance frequencies (refer to Fig. 9(a)) in comparison to the Pasternak foundation (see Fig. 9(b)). In contrast to the Winkler foundation, which solely accounts for normal stresses, the Pasternak foundation incorporates transverse and normal shear stresses. Therefore, the resonance conditions of the nanoplate are significantly impacted by the rigidity of its surrounding environment. The results of biaxial stress and the stiffness of the elastic foundation on resonance behavior may assist the development of actuators. Through the control of these parameters, actuators can be designed for fine mechanical or oscillatory activities. For example, in constructing robots, piezoelectric actuators help in creating micro-movements in motors in the robotic arms.

The relationship between the resonance frequencies and the non-local parameter for various vibrational modes of the PVDF nanoplate is illustrated in Fig. 10. For a given value of the non-local parameter, the resonance frequency of the upper modes is smaller, as indicated by the

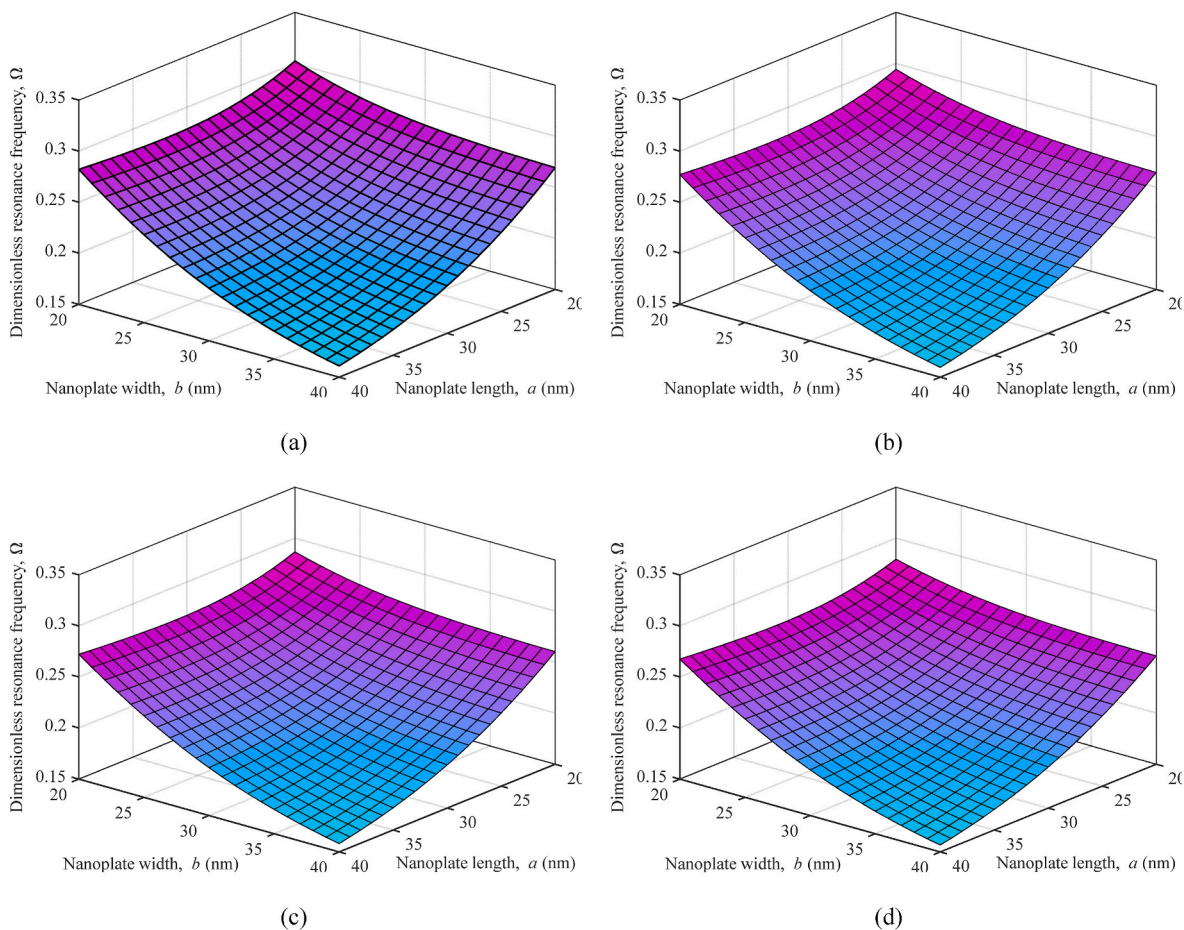


Fig. 3. Variation of dimensionless resonance frequency with width and length of the nanoplate for (a) $\mu = 0 \text{ nm}^2$, (b) $\mu = 1 \text{ nm}^2$, (c) $\mu = 2 \text{ nm}^2$, (d) $\mu = 3 \text{ nm}^2$; $h = 2 \text{ nm}$, $\kappa = \sqrt[5]{6}$, $r = 10 \text{ nm}$, $M = 10^{-19} \text{ gr}$, $V_0 = 1 \text{ volt}$, $N_x = N_y = 0$, $k_w = 0$, $k_g = 0$.

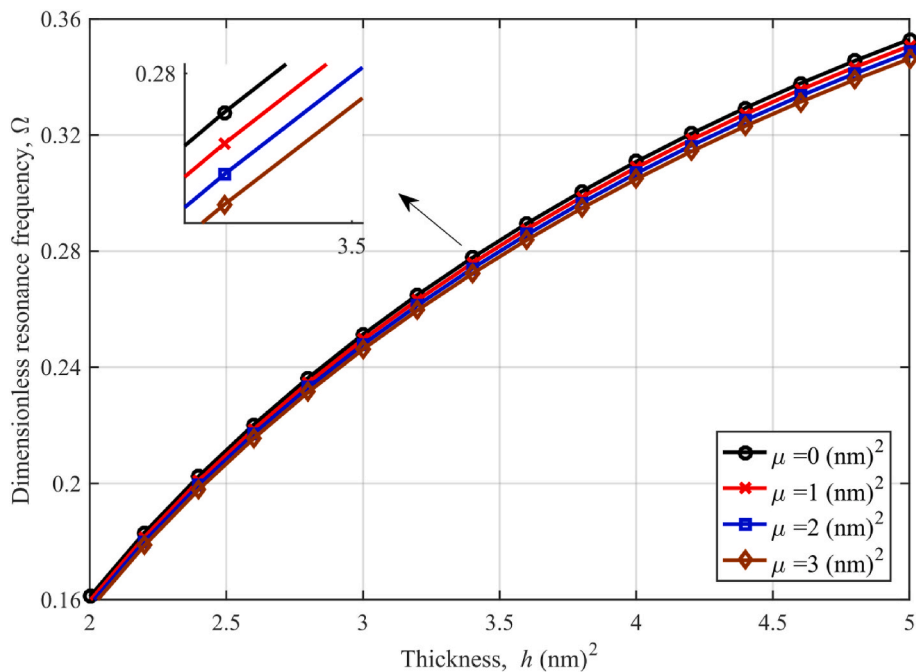


Fig. 4. Variation of dimensionless resonance frequency with nanoplate thickness for different values of non-local parameter; $a = b = 40 \text{ nm}$, $\kappa = \sqrt[5]{6}$, $r = 10 \text{ nm}$, $M = 10^{-19} \text{ gr}$, $V_0 = 1 \text{ volt}$, $N_x = N_y = 0$, $k_w = 0$, $k_g = 0$.

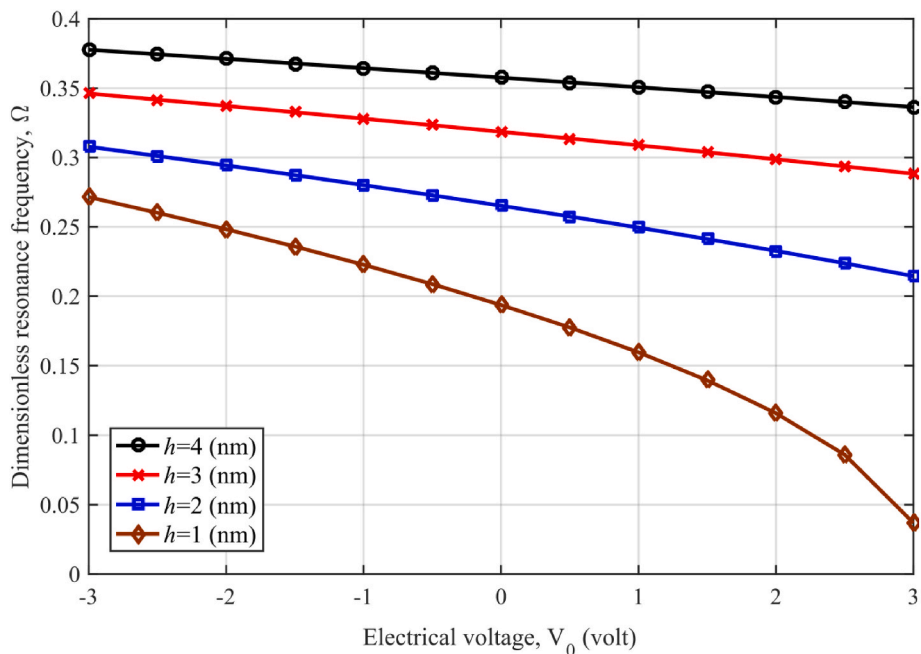


Fig. 5. Variation of dimensionless resonance frequency with electrical voltage for different values of nanoplate thickness; $a = b = 40$ nm, $\kappa = 5/6$, $r = 10$ nm, $M = 10^{-19}$ gr, $N_x = N_y = 0$, $k_w = 0$, $k_g = 0$.

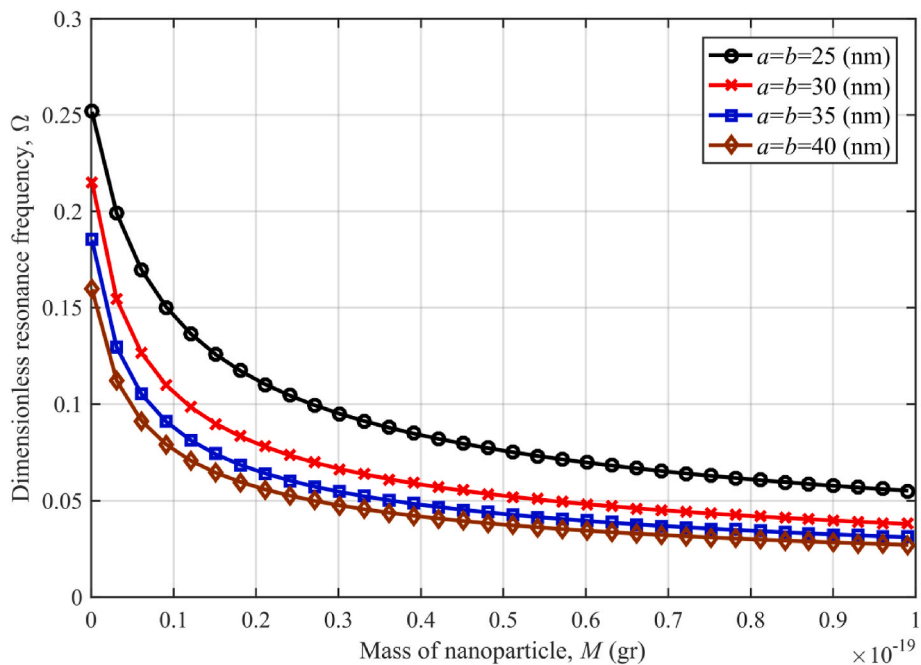


Fig. 6. Variation of dimensionless resonance frequency with mass of nanoparticle for different values of nanoplate width and length; $h = 2$ nm, $\kappa = 5/6$, $r = 10$ nm, $\mu = 1$ nm², $V_0 = 1$ volt, $N_x = N_y = 0$, $k_w = 0$, $k_g = 0$.

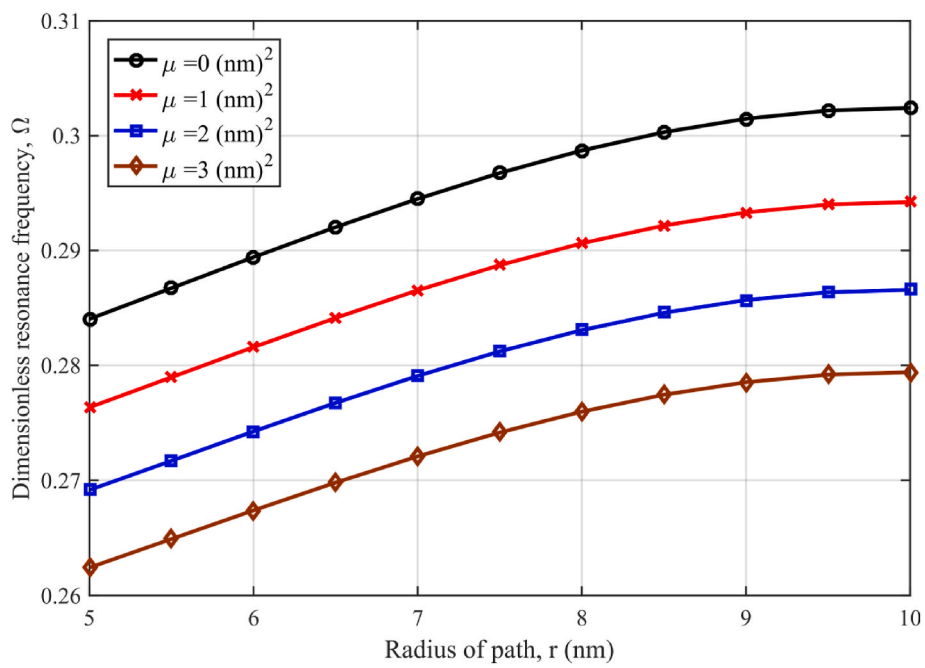


Fig. 7. Variation of dimensionless resonance frequency with the radius of the path for different values of the non-local parameter; $a = b = 20 \text{ nm}$, $h = 2 \text{ nm}$, $\kappa = \frac{5}{6}$, $M = 10^{-19} \text{ gr}$, $V_0 = 1 \text{ volt}$, $N_x = N_y = 0$, $k_w = 0$, $k_g = 0$.

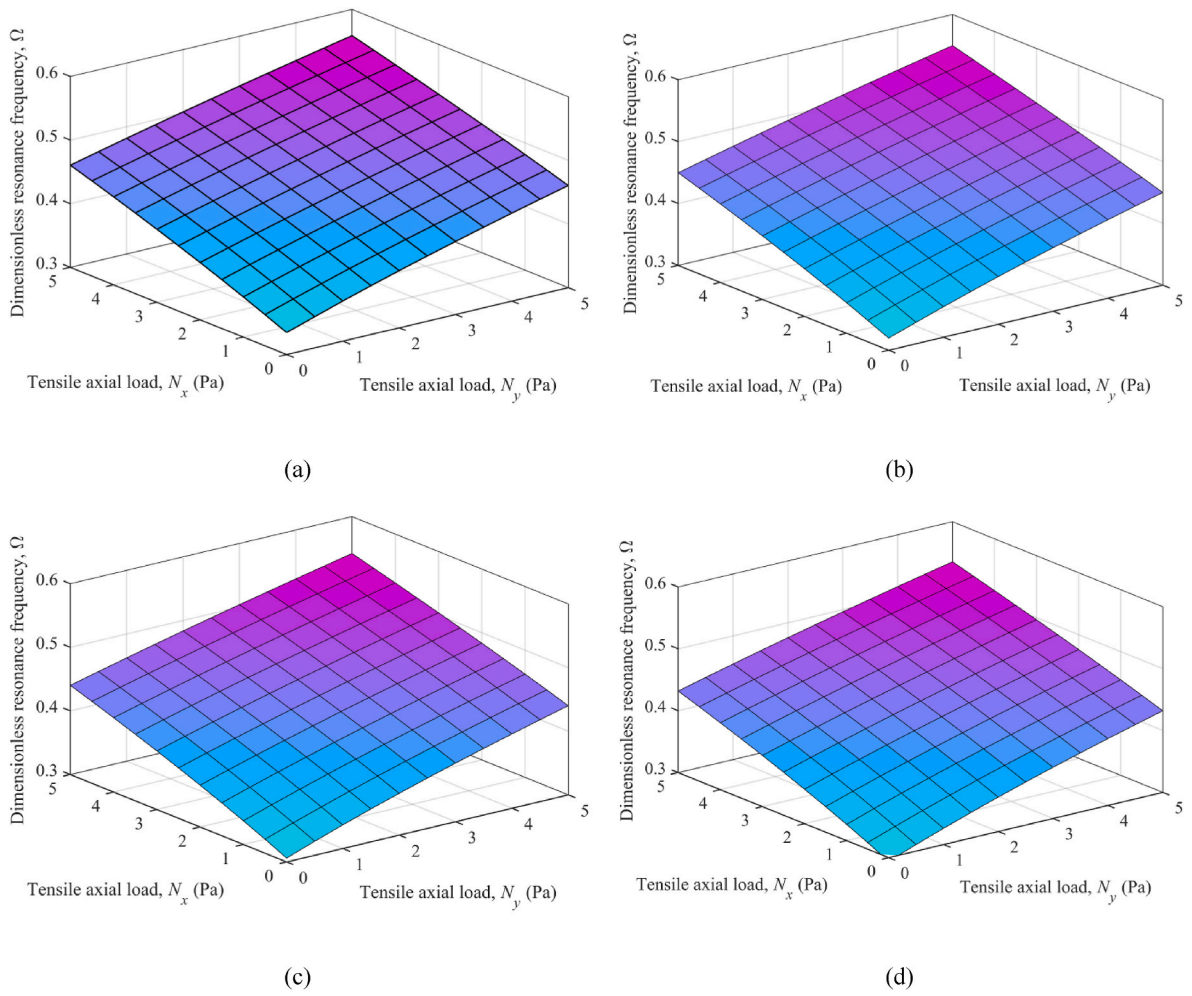
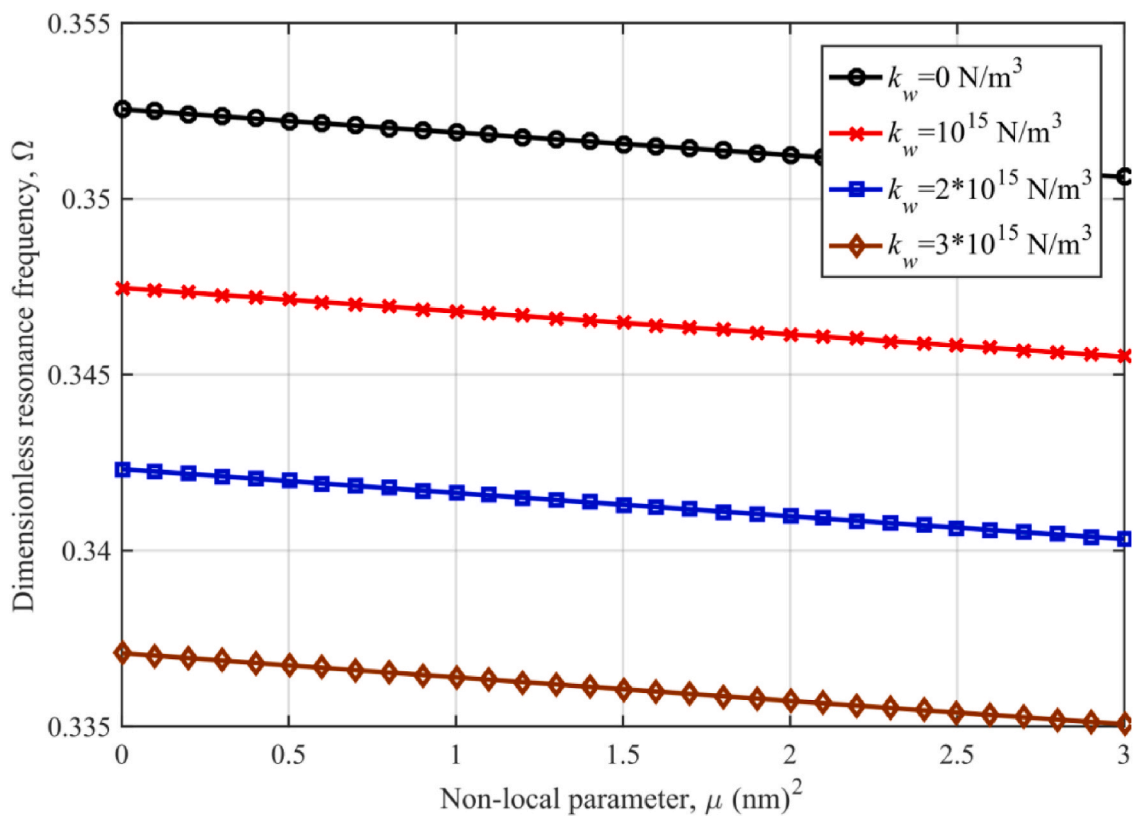
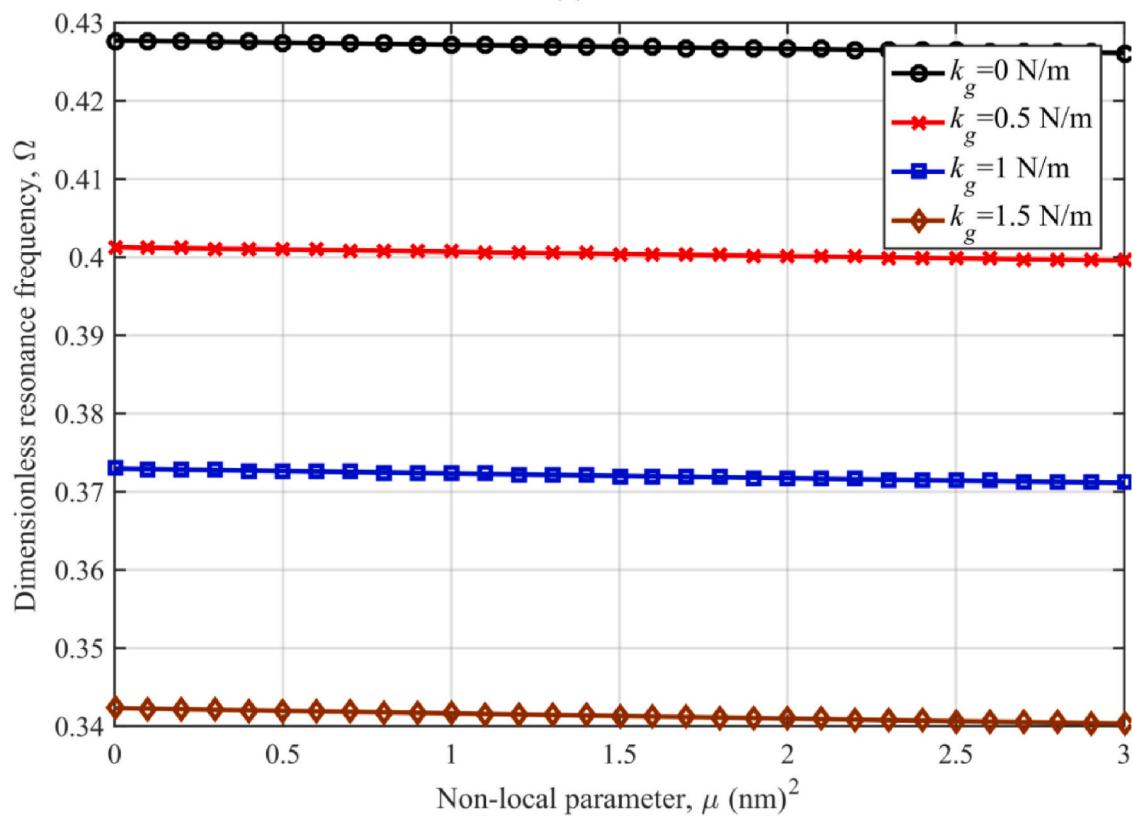


Fig. 8. Variation of dimensionless resonance frequency with tensile axial load for (a) $\mu = 0 \text{ nm}^2$, (b) $\mu = 1 \text{ nm}^2$, (c) $\mu = 2 \text{ nm}^2$, (d) $\mu = 3 \text{ nm}^2$; $a = b = 15 \text{ nm}$, $h = 2 \text{ nm}$, $\kappa = 5/6$, $r = 5 \text{ nm}$, $M = 10^{-19} \text{ gr}$, $V_0 = 1 \text{ volt}$, $k_w = 0$, $k_g = 0$.



(a)



(b)

Fig. 9. Variation of dimensionless resonance frequency with the non-local parameter for different values of (a) Winkler modulus and (b) Pasternak shear modulus; $a = b = 40 \text{ nm}$, $h = 2 \text{ nm}$, $\kappa = 5/6$, $r = 10 \text{ nm}$, $M = 10^{-19} \text{ gr}$, $V_0 = 1 \text{ volt}$, $N_x = N_y = 2 \text{ Pa}$.

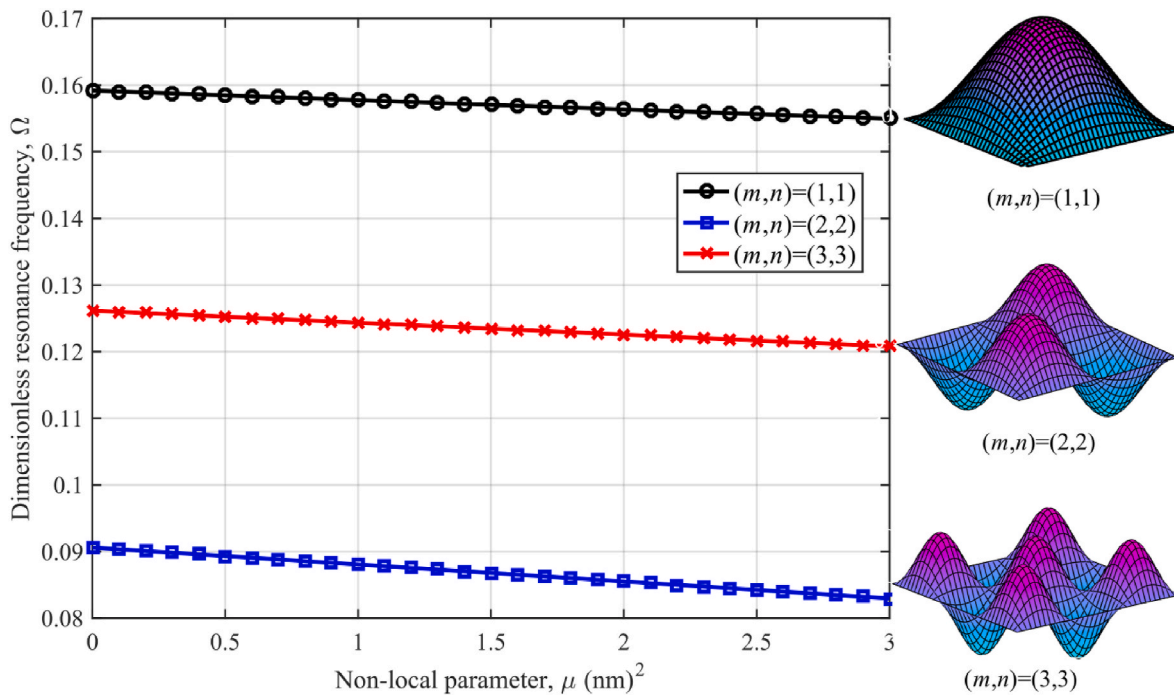


Fig. 10. Variation of dimensionless resonance frequency with the non-local parameter for different vibrational modes; $a = b = 40$ nm, $h = 2$ nm, $\kappa = 5/6$, $r = 5$ nm, $M = 10^{-19}$ gr, $V_0 = 1$ volt, $N_x = N_y = 0$, $k_w = 0$, $k_g = 0$.

plot. Moreover, an increase in the non-local parameter results in a decrease in the resonance frequencies of all modes. Moreover, non-local parameter changes can have a greater impact on the resonance frequencies of higher modes.

6. Conclusion

This study calculated the resonance frequencies of a piezoelectric polymeric nanoplate placed on an elastic substrate and exposed to electro-mechanical forces. The nanoplate was modeled using the Mindlin plate theory and the non-local piezoelectricity theory. The motion equations were obtained using the variational approach.

An investigation was conducted to examine the impact of several factors, such as the non-local parameter, dimensions of the nanoplates, the mass of the nanoparticles, excitation voltage, radius of the nanoparticle path, biaxial tensile force, stiffness of the Pasternak foundation, and mode number, on the curves depicting resonance frequency. The results revealed that increasing the non-local parameter led to a decrease in the resonance frequencies. Modifying the dimensions of the nanoplate, either by reducing its length and width or by increasing its thickness, led to an increase in the resonance frequencies. In addition, reducing the electrical voltage resulted in higher resonance frequencies, whereas providing a negative electrical voltage enhanced the rigidity of the nanostructure. Furthermore, it was inferred that the resonance frequencies of the nanostructure increased when the mass of the nanoparticle dropped or when its motion path approached the margins of the PVDF nanoplate. Furthermore, augmenting the biaxial tensile force and

stiffness of the elastic substrate resulted in a delay of the nanostructure resonance. Finally, it was noted that when the PVDF nanoplate's higher vibrational modes were stimulated, the resonance of the nanostructure's vibration started to happen at lower frequencies of the orbiting nanoparticle motion.

These findings can inform scientists about how small-scale attributes affect resonance characteristics to help design better nanostructures. This could result in developments in nanotechnology devices for instance sensors, actuators and energy harvesting devices to which resonance behaviors require stringent control.

CRediT authorship contribution statement

Narinderjit Singh Sawaran Singh: Formal analysis, Data curation, Conceptualization, Writing – original draft. **Waqed H.Hassan:** Validation, Methodology, Writing – review & editing. **Zainab Mohammed Ameen Ahmed:** Writing – original draft, Writing – review & editing. **Soheil Salahshour:** Writing – original draft, Writing – review & editing. **Younis Mohamed Atiah Al-zahy:** Conceptualization, Methodology, Software. **Mostafa Pirmoradian:** Writing – original draft, Writing – review & editing.

Declaration of competing interest

The authors declare that they have no known competing financial interests or personal relationships that could have appeared to influence the work reported in this paper.

Appendix A

Components of Eq. (27) are as follows:

$$\begin{aligned}
 M_{11} &= 1 + \pi^2 \mu \left(\frac{a^2 + b^2}{a^2 b^2} \right), M_{22} = 1 + \pi^2 \mu \left(\frac{a^2 + b^2}{a^2 b^2} \right), M_{33} = 1 + \pi^2 \mu \left(\frac{a^2 + b^2}{a^2 b^2} \right), \\
 \bar{M}_{11} &= 4 \frac{M}{\rho h a b} \cos^2 \left(\frac{\pi r}{a} \cos(\omega t) \right) \cos^2 \left(\frac{\pi r}{b} \sin(\omega t) \right) \\
 &+ 4 \frac{M}{\rho h a b} \pi^2 \mu \cos^2 \left(\frac{\pi r}{a} \cos(\omega t) \right) \cos^2 \left(\frac{\pi r}{b} \sin(\omega t) \right) \left(\frac{a^2 + b^2}{a^2 b^2} \right), \\
 \bar{C}_{11} &= 8 \frac{M \pi r}{\rho h a^2 b} \omega \sin(\omega t) \cos \left(\frac{\pi r}{a} \cos(\omega t) \right) \sin \left(\frac{\pi r}{a} \cos(\omega t) \right) \cos^2 \left(\frac{\pi r}{b} \sin(\omega t) \right) \\
 &+ 8 \frac{M \pi^3 \mu r}{\rho h a^2 b} \omega \sin(\omega t) \cos \left(\frac{\pi r}{a} \cos(\omega t) \right) \sin \left(\frac{\pi r}{a} \cos(\omega t) \right) \cos^2 \left(\frac{\pi r}{b} \sin(\omega t) \right) \left(\frac{a^2 + b^2}{a^2 b^2} \right) \\
 &- 8 \frac{M \pi r}{\rho h a b^2} \omega \cos(\omega t) \cos^2 \left(\frac{\pi r}{a} \cos(\omega t) \right) \cos \left(\frac{\pi r}{b} \sin(\omega t) \right) \sin \left(\frac{\pi r}{b} \sin(\omega t) \right) \\
 &- 8 \frac{M \pi^3 \mu r}{\rho h a b^2} \omega \cos(\omega t) \cos^2 \left(\frac{\pi r}{a} \cos(\omega t) \right) \cos \left(\frac{\pi r}{b} \sin(\omega t) \right) \sin \left(\frac{\pi r}{b} \sin(\omega t) \right) \left(\frac{a^2 + b^2}{a^2 b^2} \right), \\
 K_{11} &= \frac{\pi^2 \kappa}{\rho} \left(\frac{C_{44} a^2 + C_{55} b^2}{a^2 b^2} \right) + \frac{k_w}{\rho h} + \frac{k_w \pi^2 \mu}{\rho h} \left(\frac{a^2 + b^2}{a^2 b^2} \right) + \frac{k_g \pi^2}{\rho h} \left(\frac{a^2 + b^2}{a^2 b^2} \right) + \frac{k_g \pi^4 \mu}{\rho h} \left(\frac{a^2 + b^2}{a^2 b^2} \right)^2 \\
 &+ \frac{\pi^2 N_x}{\rho h a^2} + \frac{\pi^4 \mu N_x}{\rho h a^2} \left(\frac{a^2 + b^2}{a^2 b^2} \right) + \frac{\pi^2 N_y}{\rho h b^2} + \frac{\pi^4 \mu N_y}{\rho h b^2} \left(\frac{a^2 + b^2}{a^2 b^2} \right) + \frac{2 \pi^2 V_0 e_{31}}{\rho h a^2} \\
 &+ \frac{2 \pi^4 \mu V_0 e_{31}}{\rho h a^2} \left(\frac{a^2 + b^2}{a^2 b^2} \right) + \frac{2 \pi^2 V_0 e_{32}}{\rho h b^2} + \frac{2 \pi^4 \mu V_0 e_{32}}{\rho h b^2} \left(\frac{a^2 + b^2}{a^2 b^2} \right), \\
 K_{12} &= \frac{\pi \kappa C_{55}}{\rho a}, K_{13} = \frac{\pi \kappa C_{44}}{\rho b}, K_{14} = - \left[\frac{2 \pi \kappa e_{15}}{\rho a^2} + \frac{2 \pi \kappa e_{24}}{\rho b^2} \right], \\
 K_{21} &= \frac{12 \pi \kappa C_{55}}{\rho h^2 a}, K_{22} = \frac{\pi^2 C_{11}}{\rho a^2} + \frac{\pi^2 C_{66}}{\rho b^2} + \frac{12 \pi \kappa C_{55}}{\rho h^2}, K_{23} = \frac{\pi^2 C_{12}}{\rho a b} + \frac{\pi^2 C_{66}}{\rho a b}, \\
 K_{24} &= - \left[\frac{24 e_{31}}{\rho h^2 a} + \frac{24 \kappa e_{15}}{\rho h^2 a} \right], K_{31} = \frac{12 \pi \kappa C_{44}}{\rho h^2 b}, K_{32} = \frac{\pi^2 C_{12}}{\rho a b} + \frac{\pi^2 C_{66}}{\rho a b}, \\
 K_{33} &= \frac{\pi^2 C_{11}}{\rho b^2} + \frac{\pi^2 C_{66}}{\rho a^2} + \frac{12 \pi \kappa C_{44}}{\rho h^2}, K_{34} = - \left[\frac{24 e_{32}}{\rho h^2 b} + \frac{24 \kappa e_{24}}{\rho h^2 b} \right], \\
 K_{41} &= \frac{4 \pi h e_{15}}{a^2} + \frac{4 \pi h e_{24}}{b^2}, K_{42} = \frac{4 h e_{15}}{a} + \frac{4 h e_{31}}{a}, K_{43} = \frac{4 h e_{24}}{b} + \frac{4 h e_{32}}{b},
 \end{aligned}$$

$$\begin{aligned}
K_{44} &= \frac{\pi^2 \epsilon_{33}}{h} + \frac{\pi^2 h \epsilon_{22}}{b^2} + \frac{\pi^2 h \epsilon_{11}}{a^2}, \\
\bar{K}_{11} &= -4 \frac{M\pi^2 r^2}{\rho h a^3 b} \omega^2 \sin^2(\omega t) \cos^2\left(\frac{\pi r}{a} \cos(\omega t)\right) \cos^2\left(\frac{\pi r}{b} \sin(\omega t)\right) \\
&- 4 \frac{M\pi^4 \mu r^2}{\rho h a^3 b} \omega^2 \sin^2(\omega t) \cos^2\left(\frac{\pi r}{a} \cos(\omega t)\right) \cos^2\left(\frac{\pi r}{b} \sin(\omega t)\right) \left(\frac{a^2 + b^2}{a^2 b^2}\right) \\
&- 4 \frac{m\pi^2 r^2}{\rho h a b^3} \omega^2 \cos^2(\omega t) \cos^2\left(\frac{\pi r}{a} \cos(\omega t)\right) \cos^2\left(\frac{\pi r}{b} \sin(\omega t)\right) \\
&- 4 \frac{M\pi^4 \mu r^2}{\rho h a b^3} \omega^2 \cos^2(\omega t) \cos^2\left(\frac{\pi r}{a} \cos(\omega t)\right) \cos^2\left(\frac{\pi r}{b} \sin(\omega t)\right) \left(\frac{a^2 + b^2}{a^2 b^2}\right) \\
&- 8 \frac{M\pi^2 r^2}{\rho h a^2 b^2} \omega^2 \sin(\omega t) \cos(\omega t) \sin\left(\frac{\pi r}{a} \cos(\omega t)\right) \sin\left(\frac{\pi r}{b} \sin(\omega t)\right) \\
&\cos\left(\frac{\pi r}{a} \cos(\omega t)\right) \cos\left(\frac{\pi r}{b} \sin(\omega t)\right) - 8 \frac{M\pi^4 \mu r^2}{\rho h a^2 b^2} \omega^2 \sin(\omega t) \cos(\omega t) \sin\left(\frac{\pi r}{a} \cos(\omega t)\right) \\
&\sin\left(\frac{\pi r}{b} \sin(\omega t)\right) \cos\left(\frac{\pi r}{a} \cos(\omega t)\right) \cos\left(\frac{\pi r}{b} \sin(\omega t)\right) \left(\frac{a^2 + b^2}{a^2 b^2}\right) \\
&+ 4 \frac{M\pi r}{\rho h a^2 b} \omega^2 \cos(\omega t) \cos\left(\frac{\pi r}{a} \cos(\omega t)\right) \sin\left(\frac{\pi r}{a} \cos(\omega t)\right) \cos^2\left(\frac{\pi r}{b} \sin(\omega t)\right) \\
&+ 4 \frac{M\pi^3 \mu r}{\rho h a^2 b} \omega^2 \cos(\omega t) \cos\left(\frac{\pi r}{a} \cos(\omega t)\right) \sin\left(\frac{\pi r}{a} \cos(\omega t)\right) \cos^2\left(\frac{\pi r}{b} \sin(\omega t)\right) \left(\frac{a^2 + b^2}{a^2 b^2}\right) \\
&+ 4 \frac{M\pi r}{\rho h a b^2} \omega^2 \sin(\omega t) \cos^2\left(\frac{\pi r}{a} \cos(\omega t)\right) \cos\left(\frac{\pi r}{b} \sin(\omega t)\right) \sin\left(\frac{\pi r}{b} \sin(\omega t)\right) \\
&+ 4 \frac{M\pi^3 \mu r}{\rho h a b^2} \omega^2 \sin(\omega t) \cos^2\left(\frac{\pi r}{a} \cos(\omega t)\right) \cos\left(\frac{\pi r}{b} \sin(\omega t)\right) \sin\left(\frac{\pi r}{b} \sin(\omega t)\right) \left(\frac{a^2 + b^2}{a^2 b^2}\right), \\
\bar{F}_1 &= \frac{4Mg}{\rho h a b} \cos\left(\frac{\pi r}{a} \cos(\omega t)\right) \cos\left(\frac{\pi r}{b} \sin(\omega t)\right).
\end{aligned} \tag{A.1}$$

Appendix B

The dimensionless quantities are introduced as follows:

$$\begin{aligned}
 k_w^* &= \frac{k_w a^2 b^2}{\pi^2 \kappa h (a^2 C_{44} + b^2 C_{55})}, k_g^* = \frac{k_g (a^2 + b^2)}{\kappa h (a^2 C_{44} + b^2 C_{55})}, \\
 N_x^* &= \frac{N_x b^2}{\kappa h (a^2 C_{44} + b^2 C_{55})}, N_y^* = \frac{N_y a^2}{\kappa h (a^2 C_{44} + b^2 C_{55})}, \\
 Q_1 &= \frac{e_{31} V_0 b^2}{\kappa h (a^2 C_{44} + b^2 C_{55})}, Q_2 = \frac{e_{32} V_0 a^2}{\kappa h (a^2 C_{44} + b^2 C_{55})}, \\
 T_1 &= \frac{C_{55} a b^2}{\pi \sqrt{ab} (a^2 C_{44} + b^2 C_{55})}, T_2 = \frac{C_{44} a^2 b}{\pi \sqrt{ab} (a^2 C_{44} + b^2 C_{55})}, \\
 T_3 &= \frac{C_{11} b^2}{\kappa (a^2 C_{44} + b^2 C_{55})}, T_4 = \frac{C_{66} a^2}{\kappa (a^2 C_{44} + b^2 C_{55})}, \\
 T_5 &= \frac{C_{55} a^2 b^2}{\pi h^2 (a^2 C_{44} + b^2 C_{55})}, T_6 = \frac{C_{12} ab}{\kappa (a^2 C_{44} + b^2 C_{55})}, \\
 T_7 &= \frac{C_{66} ab}{\kappa (a^2 C_{44} + b^2 C_{55})}, T_8 = \frac{C_{55} a b^2 \sqrt{ab}}{\pi h^2 (a^2 C_{44} + b^2 C_{55})}, \\
 T_9 &= \frac{C_{11} a^2}{\kappa (a^2 C_{44} + b^2 C_{55})}, T_{10} = \frac{C_{66} b^2}{\pi h^2 (a^2 C_{44} + b^2 C_{55})}, \\
 T_{11} &= \frac{C_{44} a^2 b^2}{\pi h^2 (a^2 C_{44} + b^2 C_{55})}, T_{12} = \frac{C_{44} a^2 b \sqrt{ab}}{\pi h^2 (a^2 C_{44} + b^2 C_{55})}, \\
 A_1 &= \sqrt{\frac{C_{44}}{C_{11}}}, A_2 = \sqrt{\frac{C_{55}}{C_{11}}}, E_1 = \frac{\sqrt{C_{44} \epsilon_{11}}}{e_{15}}, E_2 = \frac{\sqrt{C_{55} \epsilon_{11}}}{e_{15}}, \\
 E_3 &= \frac{\sqrt{C_{44} \epsilon_{11}}}{e_{24}}, E_4 = \frac{\sqrt{C_{55} \epsilon_{11}}}{e_{24}}, E_5 = \frac{\sqrt{C_{44} \epsilon_{11}}}{e_{31}}, E_6 = \frac{\sqrt{C_{55} \epsilon_{11}}}{e_{31}}, \\
 E_7 &= \frac{\sqrt{C_{44} \epsilon_{11}}}{e_{32}}, E_8 = \frac{\sqrt{C_{55} \epsilon_{11}}}{e_{32}}, E_9 = \frac{\sqrt{C_{11} \epsilon_{33}}}{e_{24}}, E_{10} = \frac{\sqrt{C_{11} \epsilon_{33}}}{e_{15}}, \\
 E_{11} &= \frac{\sqrt{C_{11} \epsilon_{33}}}{e_{31}}, E_{12} = \frac{\sqrt{C_{11} \epsilon_{33}}}{e_{32}}, \Xi_1 = \sqrt{\frac{\epsilon_{33}}{\epsilon_{11}}}, \Xi_2 = \sqrt{\frac{\epsilon_{22}}{\epsilon_{33}}}, \Xi_3 = \sqrt{\frac{\epsilon_{11}}{\epsilon_{33}}}, \\
 g^* &= \frac{g}{\pi^2 \kappa \sqrt{ab} \left(\frac{C_{55}}{a^2} + \frac{C_{44}}{b^2} \right)}, \alpha = \frac{M}{\rho h a b}, \mu^* = \frac{\mu}{a b}, a_r = \frac{a}{b}, \\
 \tau &= \omega t, \tilde{W}_{11} = \frac{W_{11}}{\sqrt{ab}}, \tilde{\psi}_{x11} = \psi_{x11}, \tilde{\psi}_{y11} = \psi_{y11}, \tilde{\Phi}_{11} = \frac{\Phi_{11}}{\sqrt{\frac{C_{11}}{\epsilon_{11}} ab}}, \\
 \zeta &= \frac{r}{a}, \eta = \frac{r}{b}, r_a = \frac{h}{a}, r_b = \frac{h}{b}, \Omega = \frac{\omega}{\pi \sqrt{\frac{\kappa}{\rho} \left(\frac{C_{55}}{a^2} + \frac{C_{44}}{b^2} \right)}}.
 \end{aligned} \tag{B.1}$$

The dimensionless form of Eq. (27) is:

$$\left(\Omega^2 \begin{bmatrix} \tilde{M}_{11} & 0 & 0 & 0 \\ 0 & \tilde{M}_{22} & 0 & 0 \\ 0 & 0 & \tilde{M}_{33} & 0 \\ 0 & 0 & 0 & 0 \end{bmatrix} + \alpha \Omega^2 \begin{bmatrix} \widehat{M}_{11}(\tau) & 0 & 0 & 0 \\ 0 & 0 & 0 & 0 \\ 0 & 0 & 0 & 0 \\ 0 & 0 & 0 & 0 \end{bmatrix} \right) \begin{Bmatrix} \tilde{W}_{11}'' \\ \tilde{\psi}_{x11}'' \\ \tilde{\psi}_{y11}'' \\ \tilde{\Phi}_{11}'' \end{Bmatrix} + \alpha \Omega^2 \begin{bmatrix} \widehat{C}_{11}(\tau) & 0 & 0 & 0 \\ 0 & 0 & 0 & 0 \\ 0 & 0 & 0 & 0 \\ 0 & 0 & 0 & 0 \end{bmatrix} \begin{Bmatrix} \tilde{W}_{11}' \\ \tilde{\psi}_{x11}' \\ \tilde{\psi}_{y11}' \\ \tilde{\Phi}_{11}' \end{Bmatrix} + \left(\begin{bmatrix} \tilde{K}_{11} & \tilde{K}_{12} & \tilde{K}_{13} & \tilde{K}_{14} \\ \tilde{K}_{21} & \tilde{K}_{22} & \tilde{K}_{23} & \tilde{K}_{24} \\ \tilde{K}_{31} & \tilde{K}_{32} & \tilde{K}_{33} & \tilde{K}_{34} \\ \tilde{K}_{41} & \tilde{K}_{42} & \tilde{K}_{43} & \tilde{K}_{44} \end{bmatrix} + \alpha \Omega^2 \begin{bmatrix} \widehat{K}_{11}(\tau) & 0 & 0 & 0 \\ 0 & 0 & 0 & 0 \\ 0 & 0 & 0 & 0 \\ 0 & 0 & 0 & 0 \end{bmatrix} \right) \begin{Bmatrix} \tilde{W}_{11} \\ \tilde{\psi}_{x11} \\ \tilde{\psi}_{y11} \\ \tilde{\Phi}_{11} \end{Bmatrix} = \alpha \begin{Bmatrix} \widehat{F}_1(\tau) \\ 0 \\ 0 \\ 0 \end{Bmatrix}, \tag{B.2}$$

Where the prime superscript signifies the derivative about dimensionless time τ . The matrix components are represented as follows:

$$\begin{aligned} \tilde{M}_{11} &= 1 + \pi^2 \mu^* \left(\frac{1 + a_r^2}{a_r} \right), \tilde{M}_{22} = 1 + \pi^2 \mu^* \left(\frac{1 + a_r^2}{a_r} \right), \tilde{M}_{33} = 1 + \pi^2 \mu^* \left(\frac{1 + a_r^2}{a_r} \right), \\ \widehat{M}_{11}(\tau) &= 4 \cos^2(\pi \zeta \cos(\tau)) \cos^2(\pi \eta \sin(\tau)) + 4 \pi^2 \mu^* \cos^2(\pi \zeta \cos(\tau)) \cos^2(\pi \eta \sin(\tau)) \left(\frac{1 + a_r^2}{a_r} \right), \\ \widehat{C}_{11}(\tau) &= 8 \pi \zeta \sin(\tau) \cos(\pi \zeta \cos(\tau)) \sin(\pi \zeta \cos(\tau)) \cos^2(\pi \eta \sin(\tau)) \\ &+ 8 \pi^3 \mu^* \zeta \sin(\tau) \cos(\pi \zeta \cos(\tau)) \sin(\pi \zeta \cos(\tau)) \cos^2(\pi \eta \sin(\tau)) \left(\frac{1 + a_r^2}{a_r} \right) \\ &- 8 \pi \eta \cos(\tau) \cos^2(\pi \zeta \cos(\tau)) \cos(\pi \eta \sin(\tau)) \sin(\pi \eta \sin(\tau)) \\ &- 8 \pi^3 \mu^* \eta \cos(\tau) \cos^2(\pi \zeta \cos(\tau)) \cos(\pi \eta \sin(\tau)) \sin(\pi \eta \sin(\tau)) \left(\frac{1 + a_r^2}{a_r} \right), \\ \tilde{K}_{11} &= 1 + k_w^* + \pi^2 k_w^* \mu^* \left(\frac{1 + a_r^2}{a_r} \right) + k_g^* + \pi^2 k_g^* \mu^* \left(\frac{1 + a_r^2}{a_r} \right) + N_x^* + \pi^2 N_x^* \mu^* \left(\frac{1 + a_r^2}{a_r} \right) \\ &+ N_y^* + \pi^2 N_y^* \mu^* \left(\frac{1 + a_r^2}{a_r} \right) + 2Q_1 + 2\pi^2 Q_1 \mu^* \left(\frac{1 + a_r^2}{a_r} \right) + 2Q_2 + 2\pi^2 Q_2 \mu^* \left(\frac{1 + a_r^2}{a_r} \right), \\ \tilde{K}_{12} = T_1, \tilde{K}_{13} = T_2, \tilde{K}_{14} &= - \left[\frac{2}{\pi (a_r^2 A_1 E_1 + A_2 E_2)} + \frac{2}{\pi \left(A_1 E_3 + \frac{1}{a_r^2} A_2 E_4 \right)} \right], \\ \tilde{K}_{21} = 12T_8, \tilde{K}_{22} = T_3 + T_4 + 12T_5, \tilde{K}_{23} = T_6 + T_7, \\ \tilde{K}_{24} &= - \left[\frac{24}{\pi^2 \kappa (a_r^2 \sqrt{r_a^3 r_b} A_1 E_5 + \sqrt{r_a^3 r_b} A_2 E_6)} + \frac{24}{\pi^2 (a_r^2 \sqrt{r_a^3 r_b} A_1 E_1 + \sqrt{r_a^3 r_b} A_2 E_2)} \right], \\ \tilde{K}_{31} = 12T_{12}, \tilde{K}_{32} = T_6 + T_7, \tilde{K}_{33} = T_9 + T_{10} + 12T_{11}, \\ \tilde{K}_{34} &= - \left[\frac{24}{\pi^2 \kappa \left(\sqrt{r_a r_b^3} A_1 E_7 + \frac{\sqrt{r_a r_b^3}}{a_r} A_2 E_8 \right)} + \frac{24}{\pi^2 \left(\sqrt{r_a r_b^3} A_1 E_3 + \frac{\sqrt{r_a r_b^3}}{a_r} A_2 E_4 \right)} \right], \\ \tilde{K}_{41} &= \frac{4r_b^2}{\pi \Xi_1 E_9} + \frac{4r_a^2}{\pi \Xi_1 E_{10}}, \\ \tilde{K}_{42} &= \frac{4\sqrt{r_a^3 r_b}}{\pi^2 \Xi_1 E_{10}} + \frac{4\sqrt{r_a^3 r_b}}{\pi^2 \Xi_1 E_{11}}, \\ \tilde{K}_{43} &= \frac{4\sqrt{r_a r_b^3}}{\pi^2 \Xi_1 E_9} + \frac{4\sqrt{r_a r_b^3}}{\pi^2 \Xi_1 E_{12}}, \\ \tilde{K}_{44} &= 1 + r_b^2 \Xi_2 + r_b^2 \Xi_3, \end{aligned} \tag{B.3}$$

$$\begin{aligned}
\widehat{K}_{11}(\tau) &= -4\pi^2 \zeta^2 \sin^2(\tau) \cos^2(\pi \zeta \cos(\tau)) \cos^2(\pi \eta \sin(\tau)) \\
&- 4\pi^4 \mu^* \zeta^2 \sin^2(\tau) \cos^2(\pi \zeta \cos(\tau)) \cos^2(\pi \eta \sin(\tau)) \left(\frac{1+a_r^2}{a_r} \right) \\
&- 4\pi^2 \eta^2 \cos^2(\tau) \cos^2(\pi \zeta \cos(\tau)) \cos^2(\pi \eta \sin(\tau)) \\
&- 4\pi^4 \mu^* \eta^2 \cos^2(\tau) \cos^2(\pi \zeta \cos(\tau)) \cos^2(\pi \eta \sin(\tau)) \left(\frac{1+a_r^2}{a_r} \right) \\
&- 8\pi^2 \zeta \eta \sin(\tau) \cos(\tau) \sin(\pi \zeta \cos(\tau)) \sin(\pi \eta \sin(\tau)) \cos(\pi \zeta \cos(\tau)) \cos(\pi \eta \sin(\tau)) \\
&- 8\pi^4 \mu^* \zeta \eta \sin(\tau) \cos(\tau) \sin(\pi \zeta \cos(\tau)) \sin(\pi \eta \sin(\tau)) \cos(\pi \zeta \cos(\tau)) \cos(\pi \eta \sin(\tau)) \left(\frac{1+a_r^2}{a_r} \right) \\
&+ 4\pi \zeta \cos(\tau) \cos(\pi \zeta \cos(\tau)) \sin(\pi \zeta \cos(\tau)) \cos^2(\pi \eta \sin(\tau)) \\
&+ 4\pi^3 \mu^* \zeta \cos(\tau) \cos(\pi \zeta \cos(\tau)) \sin(\pi \zeta \cos(\tau)) \cos^2(\pi \eta \sin(\tau)) \left(\frac{1+a_r^2}{a_r} \right) \\
&+ 4\pi \eta \sin(\tau) \cos^2(\pi \zeta \cos(\tau)) \cos(\pi \eta \sin(\tau)) \sin(\pi \eta \sin(\tau)) \\
&+ 4\pi^3 \mu^* \eta \sin(\tau) \cos^2(\pi \zeta \cos(\tau)) \cos(\pi \eta \sin(\tau)) \sin(\pi \eta \sin(\tau)), \\
\widehat{F}_1 &= 4g^* \cos(\pi \zeta \cos(\tau)) \cos(\pi \eta \sin(\tau)),
\end{aligned}$$

Appendix C. Supplementary data

Supplementary data to this article can be found online at <https://doi.org/10.1016/j.cscee.2025.101125>.

Data availability

No data was used for the research described in the article.

References

- [1] H. Medjadji, M. Benlembarek, A. Boulahouache, K. Derkaoui, N. Salhi, M. Trari, Novel CoFe₂O₄/LaAlO₃ nanocomposites: an impressive photocatalyst with pn hetero-junction for improved H₂ generation under visible exposure, *Int. J. Hydrogen Energy* 88 (2024) 878–887.
- [2] K. Derkaoui, I. Bencherifa, T. Hadjersi, I. Belkhattab, K. Boukhoudim, S. Bouanik, A. Brik, M. Kechouane, M.M. Kaci, MnO₂ decorated silicon nanowires: a novel photocatalyst for improved Rhodamine B removal under visible light exposure, *Surface. Interfac.* 53 (2024) 105086.
- [3] K. Derkaoui, I. Bencherifa, Y. Mebdoua, K. Boukhoudim, T. Hadjersi, A. Chetoui, S. Naama, S. Friha, M. Kechouane, M.M. Kaci, Novel SiNWs/MnO₂/Ni (OH) 2 heterostructure as photocatalyst for efficient degradation of rhb under visible light, *J. Inorg. Organomet. Polym. Mater.* (2024) 1–18.
- [4] J.N. Reddy, *Theory and Analysis of Elastic Plates and Shells*, CRC press, 2006.
- [5] Z. Soleimani-Javid, E. Arshid, M. Khorasani, S. Amir, A. Tounsi, Size-dependent flexoelectricity-based vibration characteristics of honeycomb sandwich plates with various boundary conditions, *Adv. Nano Res* 10 (2021) 449–460.
- [6] E. Arshid, A.R. Khorshidvand, S.M. Khorandijou, The effect of porosity on free vibration of SPFG circular plates resting on visco-Pasternak elastic foundation based on CPT, FSDT and TSDT, *Struct. Eng. Mech. An Int'l J.* 70 (2019) 97–112.
- [7] E. Arshid, S. Amir, A. Loghman, Static and dynamic analyses of FG-GNPs reinforced porous nanocomposite annular micro-plates based on MSGT, *Int. J. Mech. Sci.* 180 (2020) 105656.
- [8] E. Arshid, S. Amir, A. Loghman, Thermal buckling analysis of FG graphene nanoplatelets reinforced porous nanocomposite MCST-based annular/circular microplates, *Aero. Sci. Technol.* 111 (2021) 106561.
- [9] S. Amir, Z. Soleimani-Javid, E. Arshid, Size-dependent free vibration of sandwich micro beam with porous core subjected to thermal load based on SSDBT, *ZAMM-Journal Appl. Math. Mech. für Angew. Math. und Mech.* (99) (2019) e201800334.
- [10] M. Khorasani, Z. Soleimani-Javid, E. Arshid, L. Lampani, Ö. Civalak, Thermo-elastic buckling of honeycomb micro plates integrated with FG-GNPs reinforced Epoxy skins with stretching effect, *Compos. Struct.* 258 (2021) 113430.
- [11] A.C. Eringen, *Nonlocal Continuum Field Theories*, Springer Science & Business Media, 2002.
- [12] L. Li, Y. Hu, Buckling analysis of size-dependent nonlinear beams based on a nonlocal strain gradient theory, *Int. J. Eng. Sci.* 97 (2015) 84–94.
- [13] E.O. Alzahrani, A.M. Zenkour, M. Sobhy, Small scale effect on hygro-thermo-mechanical bending of nanoplates embedded in an elastic medium, *Compos. Struct.* 105 (2013) 163–172.
- [14] M. Şimşek, H.H. Yurtcu, Analytical solutions for bending and buckling of functionally graded nanobeams based on the nonlocal Timoshenko beam theory, *Compos. Struct.* 97 (2013) 378–386.
- [15] S. Hosseini-Hashemi, M. Zare, R. Nazemnezhad, An exact analytical approach for free vibration of Mindlin rectangular nano-plates via nonlocal elasticity, *Compos. Struct.* 100 (2013) 290–299.
- [16] M. Sobhy, Generalized two-variable plate theory for multi-layered graphene sheets with arbitrary boundary conditions, *Acta Mech.* 225 (2014) 2521–2538.
- [17] A.-L. Chen, Y.-S. Wang, L.-L. Ke, Y.-F. Guo, Z.-D. Wang, Wave propagation in nanoscaled periodic layered structures, *J. Comput. Theor. Nanosci.* 10 (2013) 2427–2437.
- [18] C. Liu, L.L. Ke, Y.S. Wang, J. Yang, S. Kitipornchai, Buckling and post-buckling of size-dependent piezoelectric Timoshenko nanobeams subject to thermo-electro-mechanical loadings, *Int. J. Struct. Stabil. Dynam.* 14 (2014) 1350067.
- [19] A.S. Sayyad, Y.M. Ghugal, Bending and free vibration analysis of thick isotropic plates by using exponential shear deformation theory, *Appl. Comput. Mech.* 6 (2012).
- [20] M.A. Eltahir, F.A. Omar, W.S. Abdalla, E.H. Gad, Bending and vibrational behaviors of piezoelectric nonlocal nanobeam including surface elasticity, *Waves Random Complex Media* 29 (2019) 264–280.
- [21] M. Zarepour, S.A.H. Hosseini, A.H. Akbarzadeh, Geometrically nonlinear analysis of Timoshenko piezoelectric nanobeams with flexoelectricity effect based on Eringen's differential model, *Appl. Math. Model.* 69 (2019) 563–582.
- [22] C. Liu, L.-L. Ke, J. Yang, S. Kitipornchai, Y.-S. Wang, Nonlinear vibration of piezoelectric nanoplates using nonlocal Mindlin plate theory, *Mech. Adv. Mater. Struct.* 25 (2018) 1252–1264.
- [23] F. Ebrahimi, M. Karimiasl, R. Selvamani, Bending analysis of magneto-electro piezoelectric nanobeams system under hygro-thermal loading, *Adv. nano Res.* 8 (2020) 203–214.
- [24] O. Mazur, J. Awrejcewicz, Nonlinear vibrations of embedded nanoplates under in-plane magnetic field based on nonlocal elasticity theory, *J. Comput. Nonlinear Dynam.* 15 (12) (2020) 121001.
- [25] M. Pirmoradian, E. Torkan, N. Abdali, M. Hashemian, D. Toghraie, Thermo-mechanical stability of single-layered graphene sheets embedded in an elastic medium under action of a moving nanoparticle, *Mech. Mater.* (2019) 103248.
- [26] M. Pirmoradian, E. Torkan, D. Toghraie, Study on size-dependent vibration and stability of DWCNTs subjected to moving nanoparticles and embedded on two-parameter foundations, *Mech. Mater.* 142 (2020) 103279.
- [27] A.G. Arani, R. Kolahchi, H.G. Afshar, Dynamic analysis of embedded PVDF nanoplate subjected to a moving nanoparticle on an arbitrary elliptical path, *J. Brazilian Soc. Mech. Sci. Eng.* 37 (2015) 973–986.
- [28] A. Haghshenas, A.G. Arani, Nonlocal vibration of a piezoelectric polymeric nanoplate carrying nanoparticle via Mindlin plate theory, *Proc. Inst. Mech. Eng. Part C J. Mech. Eng. Sci.* 228 (2014) 907–920.
- [29] F. Ebrahimi, M.R. Barati, Damping vibration analysis of smart piezoelectric polymeric nanoplates on viscoelastic substrate based on nonlocal strain gradient theory, *Smart Mater. Struct.* 26 (2017) 65018.
- [30] S.A. Eftekhari, D. Toghraie, Vibration and dynamic analysis of a cantilever sandwich microbeam integrated with piezoelectric layers based on strain gradient theory and surface effects, *Appl. Math. Comput.* 419 (2022) 126867.
- [31] A. Taguet, B. Ameduri, B. Boutevin, Crosslinking of vinylidene fluoride-containing fluoropolymers, in: *Crosslinking in Materials Science*, Springer, 2005, pp. 127–211.

- [32] E. Torkan, M. Pirmoradian, M. Hashemian, On the parametric and external resonances of rectangular plates on an elastic foundation traversed by sequential masses, *Arch. Appl. Mech.* 88 (2018) 1411–1428.
- [33] S. Amir, E. Arshid, Z. Khoddami Maraghi, A. Loghman, A. Ghorbanpour Arani, Vibration analysis of magnetorheological fluid circular sandwich plates with magnetostrictive facesheets exposed to monotonic magnetic field located on visco-Pasternak substrate, *J. Vib. Control* 26 (2020) 1523–1537.
- [34] E. Arshid, A.R. Khorshidvand, Free vibration analysis of saturated porous FG circular plates integrated with piezoelectric actuators via differential quadrature method, *Thin-Walled Struct.* 125 (2018) 220–233.
- [35] C. Liu, L.-L. Ke, Y.-S. Wang, J. Yang, Nonlinear vibration of nonlocal piezoelectric nanoplates, *Int. J. Struct. Stabil. Dynam.* 15 (2015) 1540013.
- [36] E. Arshid, Z. Soleimani-Javid, S. Amir, N.D. Duc, Higher-order hygro-magneto-electro-thermomechanical analysis of FG-GNPs-reinforced composite cylindrical shells embedded in PEM layers, *Aero. Sci. Technol.* 126 (2022) 107573.
- [37] E. Arshid, S. Amir, A. Loghman, Bending and buckling behaviors of heterogeneous temperature-dependent micro annular/circular porous sandwich plates integrated by FGPEM nano-Composite layers, *J. Sandw. Struct. Mater.* 23 (2021) 3836–3877.
- [38] E. Mahmoudpour, S.H. Hosseini-Hashemi, S.A. Faghidian, Nonlinear resonant behaviors of embedded thick FG double layered nanoplates via nonlocal strain gradient theory, *Microsyst. Technol.* 25 (2019) 951–964.
- [39] E. Torkan, M. Pirmoradian, M. Hashemian, Dynamic instability analysis of moderately thick rectangular plates influenced by an orbiting mass based on the first-order shear deformation theory, *Modares Mech. Eng.* 19 (2019) 2203–2213.
- [40] J. Chen, M.K. Khabaz, M.M. Ghasemian, F.M.A. Altalbawy, A.T. Jalil, S. A. Eftekhari, M. Hashemian, D. Toghraie, Z.F. Albahash, Transverse vibration analysis of double-walled carbon nanotubes in an elastic medium under temperature gradients and electrical fields based on nonlocal Reddy beam theory, *Mater. Sci. Eng. B* 291 (2023) 116220.
- [41] M. Khaje khabaz, S.A. Eftekhari, M. Hashemian, D. Toghraie, Optimal vibration control of multi-layer micro-beams actuated by piezoelectric layer based on modified couple stress and surface stress elasticity theories, *Phys. A Stat. Mech. its Appl.* 123998 (2020).
- [42] M. Khorasani, Z. Soleimani-Javid, E. Arshid, S. Amir, Ö. Civalek, Vibration analysis of graphene nanoplatelets' reinforced composite plates integrated by piezo-electromagnetic patches on the piezo-electromagnetic media, *Waves Random Complex Media* 1–31 (2021).
- [43] S. Amir, E.M.R. Bidgoli, E. Arshid, Size-dependent vibration analysis of a three-layered porous rectangular nano plate with piezo-electromagnetic face sheets subjected to pre loads based on SSDT, *Mech. Adv. Mater. Struct.* 27 (2020) 605–619.
- [44] E. Arshid, M. Khorasani, Z. Soleimani-Javid, S. Amir, A. Tounsi, Porosity-dependent vibration analysis of FG microplates embedded by polymeric nanocomposite patches considering hygrothermal effect via an innovative plate theory, *Eng. Comput.* (2021) 1–22.
- [45] E. Torkan, M. Pirmoradian, Efficient higher-order shear deformation theories for instability analysis of plates carrying a mass moving on an elliptical path, *J. Solid Mech.* (2019), <https://doi.org/10.22034/JSM.2019.668763>.
- [46] M. Pirmoradian, E. Torkan, H. Zali, M. Hashemian, D. Toghraie, Statistical and parametric instability analysis for delivery of nanoparticles through embedded DWCNT, *Phys. A Stat. Mech. Its Appl.* 554 (2020) 123911.
- [47] M. Pirmoradian, E. Torkan, H. Karimpour, Parametric resonance analysis of rectangular plates subjected to moving inertial loads via IHB method, *Int. J. Mech. Sci.* 142 (2018) 191–215.
- [48] S. Amir, E. Arshid, Z.K. Maraghi, Free vibration analysis of magneto-rheological smart annular three-layered plates subjected to magnetic field in viscoelastic medium, *Smart Struct. Syst. An Int. J.* 25 (2020) 581–592.
- [49] Z. Khoddami Maraghi, S. Amir, E. Arshid, On the natural frequencies of smart circular plates with magnetorheological fluid core embedded between magnetostrictive patches on Kerr elastic substance, *Mech. Based Des. Struct. Mach.* 1–18 (2022).
- [50] E. Arshid, H. Arshid, S. Amir, S.B. Mousavi, Free vibration and buckling analyses of FG porous sandwich curved microbeams in thermal environment under magnetic field based on modified couple stress theory, *Arch. Civ. Mech. Eng.* 21 (2021) 1–23.
- [51] M. Pirmoradian, E. Torkan, M. Hashemian, D. Toghraie, Out-of-plane dynamic instability of nonlocal shear deformable nanoplates made of polyvinylidene fluoride materials subjected to electromechanical forces, *J. Brazilian Soc. Mech. Sci. Eng.* 43 (2021) 1–23.
- [52] E. Torkan, M. Pirmoradian, M. Hashemian, Instability inspection of parametric vibrating rectangular Mindlin plates lying on Winkler foundations under periodic loading of moving masses, *Acta Mech. Sin.* 35 (2019) 242–263.
- [53] F.R. Rofooei, A. Nikkhoo, Application of active piezoelectric patches in controlling the dynamic response of a thin rectangular plate under a moving mass, *Int. J. Solid Struct.* 46 (2009) 2429–2443.
- [54] Z.Q. Cheng, C.W. Lim, S. Kitipornchai, Three-dimensional asymptotic approach to inhomogeneous and laminated piezoelectric plates, *Int. J. Solid Struct.* 37 (2000) 3153–3175.